

Three-Dimensional Bearing-Only Target Following via Observability-Enhanced Helical Guidance

Jianan Li , Zian Ning, Shaoming He , Chang-Hun Lee , and Shiyu Zhao , *Member, IEEE*

Abstract—This paper studies the problem of air-to-air target following of micro aerial vehicles (MAVs) motivated by the application of defense against malicious MAVs. When the bearing of the target MAV has been measured by the onboard visual sensor of the pursuer MAV, the problem becomes three-dimensional (3-D) bearing-only target following, which has been rarely studied in the literature and faces some unique challenges. To solve this problem, we propose the following novel results. First, to estimate the motion of the target MAV from 3-D bearing measurements, we propose a new pseudo-linear Kalman filter, which has a concise expression and superior stability compared to the classic ones such as the extended Kalman filter and modified polar coordinate filter. Second, we propose a novel approach to analyze the observability of state estimation when only bearing information is available. While the existing approaches are applicable to 2-D and single-step time-horizon cases, ours can handle more general 3-D and multiple-step time-horizon cases. Third, based on the theoretical conclusion of our observability analysis, we design a new 3-D helical guidance law that can better exploit the additional degree of freedom in 3D. The guidance law is adapted to the quadcopter's dynamics and a low-level flight controller is designed based on geometric control. Numerical simulation results verify the superior performance of the proposed algorithms compared to the state-of-the-art ones. Flight experiments on real quadrotor platforms further show the effectiveness and robustness of the proposed algorithms in practice.

Index Terms—Aerial target following, micro aerial vehicles (MAVs), observability enhancement.

I. INTRODUCTION

WHILE micro aerial vehicles (MAVs) have been widely applied in academic and industrial domains in recent

Manuscript received 7 July 2022; accepted 27 September 2022. Date of publication 11 November 2022; date of current version 5 April 2023. This work was supported in part by the National Natural Science Foundation of China under Grant 61903308 and in part by the Hangzhou Key Technology Research and Development Program under Grant 20200416A16. This paper was recommended for publication by Associate Editor H. Garcia de Marina and Editor P. Robuffo Giordano upon evaluation of the reviewers' comments. (Corresponding author: Shiyu Zhao.)

Jianan Li is with the Department of Information Science and Electronic Engineering, Zhejiang University, Hangzhou 310027, China, and also with the School of Engineering, Westlake University, Hangzhou 310024, China (e-mail: lijianan@westlake.edu.cn).

Zian Ning and Shiyu Zhao are with the School of Engineering, Westlake University, Hangzhou 310024, China (e-mail: ningzian@westlake.edu.cn; zhaoshiyu@westlake.edu.cn).

Shaoming He is with the School of Aerospace Engineering, Beijing Institute of Technology, Beijing 100081, China (e-mail: shaoming.he@bit.edu.cn).

Chang-Hun Lee is with the Department of Aerospace Engineering, Korea Advanced Institute of Science and Technology, Daejeon 34141, South Korea (e-mail: lckdgns@kaist.ac.kr).

This article has supplementary material provided by the authors and color versions of one or more figures available at <https://doi.org/10.1109/TRO.2022.3218268>.

Digital Object Identifier 10.1109/TRO.2022.3218268



Fig. 1. Trajectories of the target and pursuer MAVs in one of our experiments. The target MAV moved with a constant speed of 5 m/s. The pursuer MAV executed the proposed bearing-only estimation and control algorithms. Each MAV has onboard lights. The photo was obtained by long-exposure photography.

years, misused and malicious MAVs have caused various problems such as disturbing airports and threatening public safety. Motivated by these problems, we study an air-to-air target following task, where a pursuer MAV should follow and maintain a desired distance to another flying target MAV. Research on this task could be potentially applied in the defense against malicious MAVs in the future.

In the problem of target following, most existing works consider the ground-to-ground [1] and air-to-ground cases [2], [3]. A few consider the 3-D air-to-air case [4], [5], which is technically more challenging as we discuss later. In [4], the authors studies the cooperative localization problem but the aerial vehicles are assumed to be installed with range-finders that are capable of measuring both the range and angles of the target, whereas in our work, only bearing information is available. The work in [4] proposes a control framework for the encirclement of a target in 3-D. At least one robot is required to know the target position and velocity information, which is a major difference compared to our work where both are not known. In the authors' previous work [6], we consider the air-to-air target following in the context of multiagent formation control. Compared to [6], this work considers a more challenging scenario where the target size is not known in advance, and hence, the distance is not directly measurable.

The first step to realize target following is to detect the target MAV by onboard sensors. Due to the payload constraints of the pursuer MAV, vision is one of the most suitable solutions for onboard sensing. Vision-based MAV detection has received increasing attention in recent years largely due to its potential applications in MAV defense systems [7]. In our recent work [8], we evaluate some state-of-the-art deep learning algorithms for MAV detection and point out that detecting unknown MAVs

robustly in complex environments remains an open problem up to now. We will specifically address the vision detection of MAVs in our future work, and merely focus on the estimation and guidance strategies in this article.

It is notable that, when the target MAV has been detected in onboard images, the relative bearing can be readily obtained based on the intrinsic parameters of the camera [9]. However, since the size of the target MAV is not known, the relative distance cannot be recovered directly. This is different from the scenarios in [6] and [10], where the target size is known. Although stereo vision could estimate target depth, its actual sensing range is usually short [11].

Given the bearing measurements of the target MAV, the consequent task becomes a bearing-only target following problem, which is the focus of this article. Such a problem faces some unique challenges as stated below.

1) The first challenge is to develop stable algorithms to estimate the motion of the target in the 3-D space from the bearing measurements. Although bearing-only motion analysis of the target has been studied by many works up to now (see Section II-A for a detailed literature review), most of these works merely focus on the 2-D case where the target and pursuer move in the same plane. This is partially because bearing-only target motion analysis was initially motivated by warship tracking over the ocean surface [12]. Up to now, the 3-D air-to-air case has not attracted sufficient attention yet. In the existing few studies on the 3-D case, the target bearing is represented by two angles: azimuth and elevation. The drawback of this representation is that it has a mathematical singularity when the elevation is equal to 90° . More importantly, the two-angle representation leads to a highly nonlinear measurement equation in the Kalman filter, causing instability or performance degeneration of the state estimation of the target.

2) The second challenge is to understand how to exploit the additional degree of freedom (DoF) in 3-D to enhance the observability of bearing-only state estimation of the target. Observability is a fundamental requirement for recovering the motion of the target from the bearing measurements. In addition to satisfying the necessary and sufficient binary condition so that the system is observable [13], the pursuer should also move adequately to enhance the degree of observability such that the motion of the target can be estimated more accurately [14]. Despite the existing studies on observability enhancement (see Section II-B for a detailed literature review), some fundamental problems in the 3-D case still remain open. In particular, observability enhancement usually relies on the Fisher information matrix (FIM) [15]. Certain metrics such as the determinant of the FIM, which could be viewed as the amount of target information retrieved from the bearing measurements, are usually maximized to achieve optimal control strategies [14], [16], [17], [18]. A well-known fundamental conclusion is that the control of the pursuer in the subsequent step should maximize the varying rate of the target bearing (e.g., [14], [16], [18], [19], [20]). This is the theoretical foundation of many existing optimal control strategies [18], [20]. Such a theoretical conclusion, however, is valid merely over a horizon of one single time step. Although it is not a severe problem for 2-D motion, it poorly exploits the

additional DoF in the 3-D case. It is, therefore, important to study the optimal control strategy over a longer horizon of multiple time steps. This problem is, however, still poorly understood and also challenging to analyze, because many metrics of FIM are no longer analytically tractable in 3-D. One can easily verify it by expanding the expression of the determinant of the FIM, as shown in (7).

3) The third challenge is how to design guidance and control strategies for the pursuer MAV to achieve the desired control objective and, in the meantime, enhance the observability. It is nontrivial to achieve the two tasks simultaneously due to coupled dynamics. In our work, the control objective is to maintain a desired constant distance between the pursuer and the target. Closely related to this problem is bearing-only target interception [18], [21], [22]. However, the existing observability-enhanced guidance strategies for target interception could not be applied in our work. That is because target interception aims to merely minimize the ultimate miss distance whereas the final interception speed is not constrained. Moreover, the existing guidance laws are designed for nonholonomic models rather than the models of quadrotor MAVs [18], [21], [22]. In these nonholonomic models, the velocity magnitude is assumed to be unchanged, and the control objective is to design lateral acceleration to adjust the velocity direction. On the other hand, observability-enhanced target following based on quadrotor MAVs has not been addressed in the literature (see Section II-C for a literature review).

This article aims to overcome the unsolved challenges identified above. Specifically, the contribution and novelty of this article are summarized as follows.

1) To estimate the motion of the target in the 3-D space, we represent the 3-D target bearing as a unit vector with measurement noise. By introducing an orthogonal projection operator, we convert the bearing measurement from a nonlinear function of the target position to a pseudolinear one, and hence, linear Kalman filtering is applicable. In this way, the bearing representation does not suffer from any singularity and, in the meantime, the estimation stability is superior compared to the two-angle nonlinear version, as verified by our simulation results.

2) For observability analysis in the 3-D space, we introduce a new optimization metric based on the FIM. This metric is equivalent to the popular one based on the FIM determinant and more analytically tractable meaning that we can obtain its explicit expression and then calculate its gradient for optimization purposes. By using a behavior-based approach, we numerically optimize the new metric over a time horizon of multiple future steps subject to motion constraints. It is revealed that the optimal strategy of the pursuer, over a horizon of multiple steps, is to move along an ellipse embedded on a 3-D sphere centered at the target. This new finding generalizes the previous results for the case of the single-step horizon, deepens our theoretical understanding of observability enhancement in 3-D, and lays the theoretical foundation for our new observability-enhanced guidance laws.

3) For the guidance and control of the pursuer quadrotor, we first design a new 3-D guidance law composed of lateral and longitudinal commands. Here, the longitudinal command is

to control the relative distance to the target MAV. The lateral one is a novel 3-D helical guidance law designed to enhance observability. This guidance law is designed based on our 3-D observability analysis. It drives the MAV to fly along 3-D helical trajectories and hence better exploits the additional DoF in the 3-D space as shown in Fig. 1. In order to track the high-level guidance command, we finally design a low-level flight control law based on the geometric control approach and incorporates the constraint that the heading of the MAV should be always aligned with the target drone.

Extensive numerical simulation results are presented to verify the effectiveness of the proposed approach. Detailed comparison with the state-of-the-art approaches demonstrates the superior performance of the proposed approach. Moreover, experiments on real quadrotor platforms have been conducted to verify the effectiveness and robustness of the proposed approach in practice.

II. RELATED WORKS

A. Review on Bearing-Only Target State Estimation

As a general estimation framework, Kalman filtering is widely used in bearing-only target estimation. One challenge of applying the Kalman filter in bearing-only estimation is the nonlinearity between the measurement and the state to be estimated. This nonlinearity would cause the estimate to be easily biased and even divergent if a conventional Cartesian coordinate-based extended Kalman filter (EKF) is utilized. Several improved methods have been proposed to alleviate the problem.

The first category of efficient approaches uses modified polar or spherical coordinates. Modified polar EKF is first proposed in [12], where the state variables are carefully selected as bearing, bearing rate, the reciprocal of range, and range rate divided by range. It separates the three observable quantities from the unobservable one (the reciprocal of range), which prevents the error covariance matrix from being ill-conditioned and ensures stability. The work in [23] extends the polar coordinate method to a spherical one to adapt to the 3-D scenario by augmenting the states with elevation with its rate. Later, the work in [24] takes acceleration estimation into consideration.

The second category is the pseudolinear Kalman filter (PLKF), which was first proposed in [25]. It solves the instability problem by transforming the nonlinear measurement equation into a pseudolinear one; thus, it is computationally efficient and suitable for real-time systems. However, this recasting makes the noise become non-Gaussian and highly correlated to the measurement matrix, which then leads to estimation bias. Nevertheless, the velocity estimate has no bias and the position bias is less than 1% when the range is relatively small [26]. The bias problem is later mitigated by introducing a modified-gain approach where the Kalman gain is calculated as a function of prior estimation only [27].

Recently, other approaches based on advanced but more complex filters, such as the particle filter [28], have been proposed. These approaches are computationally intensive and not amenable to a real-time implementation, which is critical in high-speed motion of aerial vehicles. The most recent work

is [29] where a bias-compensation PLKF is proposed. However, similar to [23], a large amount of nonlinear trigonometric functions are involved in the proposed filter, making the overall expression quite complicated, so as the calculation of covariance matrices.

In summary, most of the existing literature considers the bearing-only estimation in the 2-D scenario. When it comes to 3-D, the bearing is usually represented by two angles, which would cause potential singularity and complicate the filter design.

B. Review on Observability Analysis

Observability is a fundamental problem in bearing-only target motion analysis. The early works mainly address binary observability, which is to determine whether the system is observable or not. For example, the work in [25] constructs a matrix composed of a time series of state transition and observation matrices, and uses its rank to determine the binary observability. However, the observer motion is constrained to be rectilinear. The work in [13] establishes a rigorous observability requirement. It shows that unique tracking solutions can be obtained if and only if the accelerating own-ship satisfies a specified constraint, where the constraint is a function of acceleration and observation angles on a plane. It is later extended to the 3-D scenario in [30]. The work in [31] further generalizes the observability criteria in [13] to N th-order target dynamics.

Apart from determining whether it is observable or not, other researchers have focused on quantifying the observability. The work in [16] introduces FIM into observability analysis for the first time. Since then, the determinant of FIM has become a popular measure. For example, the recent works in [17] and [18] where eigenvalues of Cramer–Rao lower bound and the logarithm of determinant of FIM are used for constructing performance indexes maximizing observability, respectively. Geometric methods, in which they use the geometric relationship between the target and the pursuer in two consecutive time instants, are also used for deriving the measure of observability, for instance, in [19] and [20], and the results are consistent with those derived using FIM.

In summary, a popular approach for quantifying observability is to use FIM. However, most existing works only consider the 2-D scenario. Although the work in [32] considers the 3-D case, it gives an analytical observability condition only. The most relevant work is [33] which quantifies observability in 3-D. However, the sensors are assumed to be freely distributed whereas in our case, a certain spatial constraint must be added.

C. Review on Observability Enhanced Maneuvering Strategies

When bearing is the only information source of homing guidance, the commonly adopted guidance laws, such as pure pursuit guidance (PPG) and proportional navigation guidance (PNG) [34], will usually fail to estimate the state of the target thus increasing the missing rate. The main reason for the performance deterioration is the lack of observability due to the absence of range measurement as pointed out in [35]. In order to enhance observability, the pursuer must adopt certain maneuvering strategies, and we classify them into four categories.

The first category includes heuristics-based methods such as those described in [35] and [36] where an extra acceleration command is added to the classic PNG. The maneuvering frequency can be controlled by adjusting the coefficient of the maneuvering term. This extra acceleration is generally induced by the initial yaw or pitch angle.

The second category includes virtual state methods [21], [37]. The additional virtual state is usually selected as the integral of the cross-range relative to the down-range of the pursuer. The trajectory is modulated to be a weaving pattern by imposing the virtual state be zero. By changing the initial value or the number of virtual states, the weaving pattern can be modulated [37]. The advantage of this method lies in its simple structure and easy implementation on real systems.

The third category is intermittent strategy, first proposed in [38]. This scheme intentionally switches OFF the conventional guidance commands to introduce guidance errors and increase line-of-sight (LOS) rate, thus enhancing observability. The guidance command is then reactivated at the terminal homing phase. Several improved versions with adaptivity are proposed in [39], [40], [41] where the observability is evaluated first before deciding whether to increase or decrease the bearing rate. The advantage is that it can provide adequate trajectory modulation to enhance observability without wasting excessive control energy and it can be implemented in real time.

The fourth category is optimal control-based methods, where the objective functions are usually the determinant of FIM [14], [16], [42], [43]. The work in [44] proposes a linear-quadratic guidance law where observability Gramian is considered in its optimal solution. However, the optimal path has a conjugate point whose time-to-go needs to be tuned larger than the missile time-to-go by adjusting weighting parameters. Otherwise, the conjugate point may result in the algorithm to be divergent. The authors in [43] proposes an improved version of [44] where relative velocity and varying observability penalty proportional to the square of time-to-go are considered to achieve better observability. Nevertheless, they both require additional information, such as time-to-go, which in turn proposes a more demanding requirement on estimation accuracy. The recent work in [18] considers an engagement task for a cooperative target where the direction of the target's velocity is assumed to be accurately known, whereas in our tracking task we have to estimate it. The work in [45] proposes an optimal maneuvering strategy for an unknown target. However, their objective is only to estimate the state of the target while in our case we need to further maintain a desired range.

III. PROBLEM STATEMENT AND OVERVIEW

Consider a target MAV flying with constant speed in the 3-D space. Suppose a pursuer MAV, which is a quadrotor platform, could use onboard vision to detect the target and hence obtain its relative bearing. Let $p_T, v_T \in \mathbb{R}^3$ be the position and velocity of the target MAV, and $p, v \in \mathbb{R}^3$ the position and velocity of the pursuer MAV, all expressed in an inertial coordinate frame. The goal of the pursuer MAV is to approach the target from

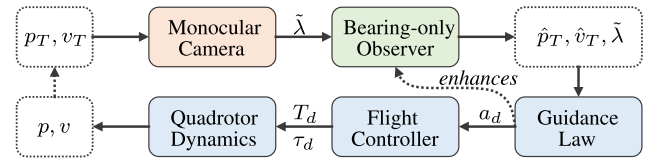


Fig. 2. Architecture of the proposed approach.

any initial distant location and then maintain a desired relative distance $r_d > 0$.

In order to achieve this goal, we design a compound system including target estimation, guidance, and flight control. The overall system architecture is shown in Fig. 2. As can be seen, the output of the vision system is a noise-corrupted bearing measurement $\tilde{\lambda}$. The first step is to design a bearing-only observer to estimate the target's position and velocity (see Section IV). Then, it is necessary to analyze the observability to the target and reveal optimal maneuvering strategies to enhance the observability (see Section V). The next step is to design a guidance law for the pursuer MAV to approach the target and, in the meantime, enhance the observability (see Section VI) from which the desired acceleration of the pursuer a_d is derived. The final step is to design the low-level flight control law including the desired thrust T_d and torque τ_d of the pursuer MAV to track the guidance command a_d (see Section VII).

IV. 3-D BEARING-ONLY TARGET ESTIMATION

This section introduces a novel bearing-only PLKF to estimate the position and velocity of the target from noisy bearing measurements in 3-D.

A. State Transition Equation

Denote the states of the target and pursuer as $x_T = [p_T^T, v_T^T]^T \in \mathbb{R}^6$ and $x_P = [p^T, v^T]^T \in \mathbb{R}^6$, respectively. Here, x_P is known and x_T is to be estimated. The discrete double-integrator dynamics of the states are described by

$$x_{T,k} = Ax_{T,k-1} + Bq_k \quad (1a)$$

$$x_{P,k} = Ax_{P,k-1} + Bu_k \quad (1b)$$

where

$$A = \begin{bmatrix} I_{3 \times 3} & \Delta t I_{3 \times 3} \\ 0_{3 \times 3} & I_{3 \times 3} \end{bmatrix}, B = \begin{bmatrix} \frac{1}{2} \Delta t^2 I_{3 \times 3} \\ \Delta t I_{3 \times 3} \end{bmatrix}$$

and Δt is the sampling time. Here, $u_k \in \mathbb{R}^3$ is the control input of the pursuer, q_k is a process noise drawn from a zero-mean normal distribution, that is, $q_k \sim \mathcal{N}(0, Q_k)$, where we assume the acceleration of the target is unknown.

Subtracting (1a) from (1b) leads to the dynamical equation of the relative state $x = x_T - x_P$:

$$x_k = Ax_{k-1} - Bu_k + Bq_k. \quad (2)$$

The term Bu_k could be calculated by $Bu_k = x_{P,k} - Ax_{P,k-1}$ according to (1b).

B. Measurement Equation

While p and p_T are the position of the pursuer and target MAVs, respectively, we know that

$$\lambda = \frac{p_T - p}{\|p_T - p\|} \quad (3)$$

is a unit vector representing the relative bearing of the target with respect to the pursuer. In our work, we use the unit vector instead of angles to represent 3-D bearings to avoid complicated trigonometric functions.

In practice, we are only able to obtain a noise-corrupted bearing, denoted as $\tilde{\lambda}$:

$$\tilde{\lambda} = \lambda + \nu \quad (4)$$

where $\nu \in \mathbb{R}^3$ is the measurement noise assumed to be normally distributed: $\nu \sim \mathcal{N}(0, \Sigma)$, $\Sigma = \sigma^2 I_{3 \times 3}$. For the details on how $\tilde{\lambda}$ is expressed in an *additive* form as in (4), interested readers can refer to Appendix.

It is noticed in (4) that $\tilde{\lambda}$ is a nonlinear function of p_T . In order to obtain a linear measurement equation, we introduce an orthogonal projection operator inspired by our previous work [46]. For any nonzero vector $g \in \mathbb{R}^3$, define

$$P_g = I_{3 \times 3} - \frac{g}{\|g\|} \frac{g^T}{\|g\|}. \quad (5)$$

The interpretation of P_g is that, for any vector $z \in \mathbb{R}^3$, its orthogonal projection onto the plane perpendicular to g is $P_g z$. The matrix P_g satisfies $P_g = P_g^T$, $P_g^2 = P_g$ and $\ker(P_g) = \text{span}(g)$ [46].

Multiplying $rP_{\tilde{\lambda}}$ on both sides of (4) gives

$$0_{3 \times 1} = P_{\tilde{\lambda}}(p_T - p) + rP_{\tilde{\lambda}}\nu$$

where $r = \|p_T - p\|$ and the left-hand side is zero because $P_{\tilde{\lambda}}\tilde{\lambda} = 0$. Thus, the nonlinear bearing function becomes a pseudolinear equation. Furthermore, since the relative state to be estimated is $x := [(p - p_T)^T, (v - v_T)^T]^T \in \mathbb{R}^6$, the final measurement equation is obtained as

$$0_{3 \times 1} = \begin{bmatrix} P_{\tilde{\lambda}} & 0_{3 \times 3} \end{bmatrix} x + rP_{\tilde{\lambda}}\nu. \quad (6)$$

Note that in (6), ν is assumed to be normally distributed and the term $rP_{\tilde{\lambda}}$ can be considered as a time-varying noise transition matrix. By inspection, we can conclude this transition depends on the true range r and the orientation of the vector $\tilde{\lambda}$. One problem for estimating the noise transition matrix is that the true range r is not known in practice, so in the filter, we replace r in (6) with a predicted one. Such replacement has been used in [29] and verified to be effective in our simulation and experimental results.

C. 3-D Bearing-Only PLKF

The steps of the proposed 3-D bearing-only observer under the framework of Kalman filter is summarized below. The prediction step is

$$\begin{aligned} \hat{x}_k^- &= A(\hat{x}_{k-1} + x_{P,k-1}) - x_{P,k} \\ P_k^- &= AP_{k-1}A^T + BQ_kB^T \end{aligned}$$

where \hat{x}_k^- and P_k^- are the priori state estimate and error covariance, respectively. The correction step is

$$\begin{aligned} K_k &= P_k^- H_k^T (H_k P_k^- H_k^T + V_k \Sigma V_k^T)^\dagger \\ \hat{x}_k &= \hat{x}_k^- - K_k H_k \hat{x}_k^- \\ P_k &= (I_{6 \times 6} - K_k H_k) P_k^- \end{aligned}$$

where $H_k = \begin{bmatrix} P_{\tilde{\lambda}_k} & 0_{3 \times 3} \end{bmatrix}$, K_k is the observer gain, $V_k = \hat{r}_k^- P_{\tilde{\lambda}_k}$ and \hat{r}_k^- is simply the norm of the first three components of \hat{x}_k^- , \hat{x}_k and P_k are the posterior state estimate and error covariance, and symbol \dagger denotes the pseudoinverse. The reason for using pseudoinverse is that the matrix $(H_k P_k^- H_k^T + V_k \Sigma V_k^T)$ is rank deficient since $P_{\tilde{\lambda}_k}$ in H_k is rank deficient. The usage of pseudoinverse in the Kalman filter is a common practice when the inverse does not exist, as shown in [47], [48], [49].

Denote z_k as the measurement in a classic Kalman filter. According to (6), it is noticeable that in our model z_k is actually $0_{3 \times 1}$. With $z_k = 0_{3 \times 1}$, the standard step of updating the posterior estimate \hat{x}_k is thus reduced as follows:

$$\hat{x}_k = \hat{x}_k^- + K_k(z_k - H_k \hat{x}_k^-) = \hat{x}_k^- - K_k H_k \hat{x}_k^-.$$

Actually, the measurement information has been implicitly contained in matrix H_k , and this is also where the name *pseudolinear* comes from because H_k is varying. In addition, the observation matrix H_k has the same mathematical expression in both 2-D and 3-D cases. Particularly, H_k can be written as $H_k = \begin{bmatrix} P_{\tilde{\lambda}_k} & 0_{d \times d} \end{bmatrix}$, where $\tilde{\lambda} \in \mathbb{R}^d$ and d is the space dimension that can be 2 or 3. By contrast, the observation matrices for common EKF methods have more complicated expressions when dimension is lifted from 2 to 3. This is how the name *uniform PLKF*, or *u-PLKF* is coined as.

V. 3-D OBSERVABILITY ENHANCEMENT

This section presents a new approach to enhancing the bearing-only observability in 3-D over a multistep horizon. The merit of this method is that it could unify the analysis of observability in both 2-D and 3-D cases and, more importantly, it extends the existing observability analysis from a single-step horizon to a multistep horizon so that the additional DoF in 3-D is better exploited.

Consider a time horizon of n steps and suppose that the bearing measurements over this time horizon are $\{\lambda_i\}_{i=k}^{k+n}$. The FIM computed from these measurements is

$$\begin{aligned} \mathcal{I}_n(p_T) &= \sum_{i=k}^{k+n} \left[\frac{\partial \lambda_i(p_T, p)}{\partial p_T} \right]^T \Sigma^{-1} \left[\frac{\partial \lambda_i(p_T, p)}{\partial p_T} \right] \\ &= \frac{1}{\sigma^2} \sum_{i=k}^{k+n} \frac{1}{r_i^2} (I_{3 \times 3} - \lambda_i \lambda_i^T) \end{aligned} \quad (7)$$

where $\lambda_i(p_T, p) = (p_T - p) / \|p_T - p\|$ is the i th bearing vector and $\partial \lambda_i(p_T, p) / \partial p_T = (I_{3 \times 3} - \lambda_i \lambda_i^T) / r_i$. In the derivation, the fact $(I_{3 \times 3} - \lambda_i \lambda_i^T)^2 = (I_{3 \times 3} - \lambda_i \lambda_i^T)$ is used.

The determinant of the FIM, representing the amount of information of the target that could be retrieved from the noisy

measurements, is widely used for observability enhancement in the 2-D or single-step horizon cases [18], [20]. However, optimizing this metric in the 3-D and the multistep horizon is challenging and has not been studied in the past since the explicit expression of this FIM determinant is nontrivial to obtain in the 3-D case, and becomes even more complicated for multiple steps (that is, $n > 2$). We present the following approach to solve these problems.

Consider a new observability metric: $J = \|\mathcal{I}_n - \bar{\lambda}I_{3 \times 3}\|_F^2$, where $\bar{\lambda}$ is the average of the eigenvalues of \mathcal{I}_n , and $\|\cdot\|_F$ denotes Frobenius norm for a matrix. It has been proven in our previous work [33] that minimizing $\|\mathcal{I}_n - \bar{\lambda}I_{3 \times 3}\|_F^2$ is equivalent to maximizing $\det(\mathcal{I}_n)$, the latter of which is a popular metric for observability enhancement. The advantage of the new metric compared to $\det(\mathcal{I}_n)$ is that it is more analytically tractable meaning we can obtain its explicit expression and conduct further analysis. Therefore, we aim to minimize $\|\mathcal{I}_n - \bar{\lambda}I_{3 \times 3}\|_F^2$. The interpretation is to minimize the diversity of the eigenvalues of \mathcal{I}_n because $\|\mathcal{I}_n - \bar{\lambda}I_{3 \times 3}\|_F^2 = 0$ when the eigenvalues of \mathcal{I}_n are equal to each other. Substituting the expression of \mathcal{I}_n in (7) into $\|\mathcal{I}_n - \bar{\lambda}I_{3 \times 3}\|_F^2$ and following the steps in [33, Sec. III] gives

$$\|\mathcal{I}_n - \bar{\lambda}I_{3 \times 3}\|_F^2 = \|G\|_F^2 - \frac{1}{3} \left(\sum_{i=1}^n \frac{1}{\sigma^2 r_i^2} \right)^2 \quad (8)$$

where

$$G = \frac{1}{\sigma^2} \sum_{i=1}^n \frac{1}{r_i^2} \lambda_i \lambda_i^T. \quad (9)$$

Before proceeding, we notice from (7) that the FIM is jointly determined by r_i and λ_i , which are the i th relative range and bearing vector. In order to determine the optimal values of r_i and λ_i , we can fix one and then calculate the other. In particular, if we fix λ_i , it is trivial to see that the optimal value of r_i is zero so that the metrics based on the FIM such as its determinant increase to infinity. However, since r_i should be no less than a desired value in the target following task, the optimal solution is that r_i should be equal to the desired distance. Similarly, we can fix r_i and then calculate the optimal values of λ_i . Since it is trivial to see that the optimal value of the range should be as small as possible, we mainly focus on determining the optimal values of bearing vectors. For the sake of simplicity, we consider the case of $r_i = r_d$, where the pursuer has already reached the desired distance. When $r_i = r_d$, minimizing $\|\mathcal{I}_n - \bar{\lambda}I_{3 \times 3}\|_F^2$ is equivalent to minimizing $\|G\|_F^2$ as can be seen from (8). Moreover, the expression of $\|G\|_F^2$ is

$$\|G\|_F^2 = \frac{1}{\sigma^4 r_d^4} \left(n + 2 \sum_{i=1}^n \sum_{j=1, j \neq i}^n (\lambda_i^T \lambda_j)^2 \right). \quad (10)$$

While minimizing $\|G\|_F^2$, we need also consider some practical constraints. In particular, the constrained optimization problem we aim to solve is

$$\min_{\lambda_i} \|G\|_F^2 \quad (11a)$$

$$\text{s.t. } \|\lambda_i - \lambda_{i-1}\| \leq \delta \quad (11b)$$

$$\lambda_i \in S. \quad (11c)$$

The two constraints in (11b) and (11c) are discussed as follows. First, the constraint in (11b) is the continuity constraint. In particular, since the multiple observations $\{\lambda_i\}_{i=1}^n$ are obtained by a single observer over consequent time steps, adjacent observations should not be too far away from each other. Here, δ in (11b) is an upper bound. Note when $i = 1$, the continuity constraint is $\|\lambda_1 - \lambda_n\| \leq \delta$ forming a loop such that the observer can have a periodic movement. Second, the constraint in (11c) is the motion constraint of the observer. In particular, when pursuing a target, the observer may follow behind the target instead of moving to the front. Hence, we hope to optimize the motion of the observer within a confined space S . Typically, we introduce a set of planes carrying repulsive pseudoforces to repel the particles into the specified region S in (11c).

It is notable that we do not treat the energy consumption of the pursuer MAV as a constraint. That is because, in applications such as defending malicious MAVs, successfully defending the target within a short time is much more important than reducing energy consumption.

The constrained optimization problem is nonconvex and challenging to solve. We propose the following numerical method to solve it from a dynamic control perspective. The numerical method in (12) is a *behavior-based* method, which is inherently heuristic. The idea of this kind of methods is to introduce pseudoforces to satisfy the constraints and has been applied in many motion coordination tasks such as [50] and [51]. In particular, consider a system composing of n particles moving on the surface of a unit sphere centered at the target. Each particle represents an observation; thus, the vector from the position of the i th particle to the position of the target is the i th bearing vector λ_i . Our idea is to apply the following pseudoforces to steer the particles moving from an initial configuration to a final configuration so that $\|G\|_F^2$ is minimized while the constraints are satisfied:

$$f_{i,1} = -k_g P_{\lambda_i} G \lambda_i \quad (12a)$$

$$f_{i,2} = k_m P_{\lambda_i} (\lambda_{i-1} - \lambda_i) \quad (12b)$$

$$f_{i,3} = \sum_{j=1}^{n_p} k_{b,j} P_{\lambda_i} \hat{n}_j / d_{i,j} \quad (12c)$$

where $\hat{n}_j \in \mathbb{R}^3$ is the unit direction vector for the j th plane creating repulsive pseudoforces to the particles, $d_{i,j} \in \mathbb{R}^+$ is the distance to the plane, $k_g, k_m, k_{b,j} \in \mathbb{R}^+$ are gains, and n_p is the number of planes. The three pseudoforces are explained as follows.

1) The first pseudoforce $f_{i,1}$ is the gradient-descent pseudoforce designed to minimize $\|G\|_F^2$. To see why $f_{i,1}$ can minimize $\|G\|_F^2$, consider the Lyapunov function $V = \|G\|_F^2/2$. The time derivative of V is

$$\begin{aligned} \dot{V} &= \text{tr}(G\dot{G}) \\ &= \frac{1}{\sigma^4 r_d^4} \text{tr} \left(\sum_{i=1}^n (\lambda_i \lambda_i^T) \cdot \sum_{i=1}^n (\dot{\lambda}_i \lambda_i^T + \lambda_i \dot{\lambda}_i^T) \right) \\ &= \frac{1}{\sigma^2 r_d^2} \sum_{i=1}^n (\lambda_i^T G \dot{\lambda}_i + \dot{\lambda}_i^T G \lambda_i). \end{aligned}$$

Substituting $\dot{\lambda}_i = f_{i,1}$ into \dot{V} gives

$$\dot{V} = \frac{-k_g}{\sigma^2 r_d^2} \sum_{i=1}^n \|P_{\lambda_i} G \lambda_i\|^2 \leq 0.$$

Define set $\Omega = \{\lambda_i : \dot{V}(\lambda_i) = 0, i = 1, \dots, n\}$, which indicates the result $\dot{\lambda}_i = P_{\lambda_i} G \lambda_i = 0$; thus, the set Ω is itself invariant. Invoking LaSalle's invariance principle [52], we conclude that $\{\lambda_i\}_{i=1}^n$ asymptotically converges to set Ω , which also indicates the decreasing of V .

2) The second one $f_{i,2}$ is designed to satisfy the continuity constraint in (11b). To satisfy this constraint, each particle is assumed to be attracted by its adjacent particle with the pseudoforce $f_{i,2}$ as a soft motion constraint. Here, a proportion-like controller is used that the attractive pseudoforce is proportional to their position error $\lambda_{i-1} - \lambda_i$. The attraction is then projected onto the surface of the sphere to maintain the range to the target as indicated by the multiplication of P_{λ_i} .

3) The third one $f_{i,3}$ is designed to satisfy the motion constraint in (11c). By creating repulsive pseudoforces generated by a set of planes in space, the particles can be confined in a specified region. The repulsive pseudoforce between particle i and plane j is designed to be inversely proportional to their distance $d_{i,j}$, and particle i receives a total of n_p planes' repulsive pseudoforces. The particles can never cross the border of the confined space as the repulsion will tend to infinity when the distance approaches zero, which is manifested by the division of $d_{i,j}$. Same to the attraction, it is again projected onto the surface of the sphere to maintain the range.

Extensive numerical simulation has verified the effectiveness of the proposed optimization method. More importantly, it is noticed that the optimal solution to (11) form a circle or a curved ellipse fitted on the surface of the unit sphere in the presence of spatial constraints. Illustrative examples are given in Figs. 3 and 4.

Fig. 3 shows the convergence procedure to the solution of the optimization problem in (11) by our numerical method. We first generate ten particles arbitrarily distributed on the surface of a unit sphere, as shown in Fig. 3(a). It is remarked that the selection of the number of particles n is mainly dependent on the observation frequency. In addition, one repulsive plane is placed passing through the point $[-1, 0, 0]^T$ with its normal $\hat{n}_1 = [1, 0, 0]^T$, which is to limit particles to move only in the half-space. The gains are set to be $k_g = k_{b,1} = 1$, and $k_m = 5$. Under the action of the pseudoforces described in (12a)–(12c), the system will gradually reach a dynamic equilibrium state, as shown in Fig. 3(d). In the dynamic equilibrium state, all the particles revolve around in a circle.

Fig. 4 shows the optimal solutions when the magnitude of the pseudoforces are tuned. By increasing $k_{b,1}$, we can increase the repulsion to confine the particles in a smaller region corresponding to the case when the maneuverability of the observer is low. The case for $k_{b,1} = 10$ is shown in Fig. 4(a). Nevertheless, the result is consistent that a circular distribution will reach the optimal observability. In Fig. 4(b), two more repulsive planes are added passing through $[0, 0, 1]^T$ and $[0, 0, -1]^T$ with their normals $\hat{n}_2 = [0, 0, -1]^T$ and $\hat{n}_3 = [0, 0, 1]^T$, where

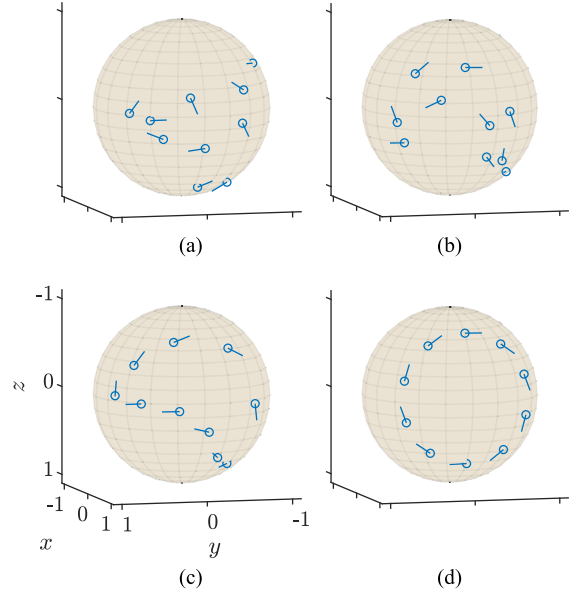


Fig. 3. Convergence process to the solution of (11) by our numerical method. The arrows of the particles represent velocity. (a) $t = 0$ s. (b) $t = 1$ s. (c) $t = 2$ s. (d) $t = 10$ s.

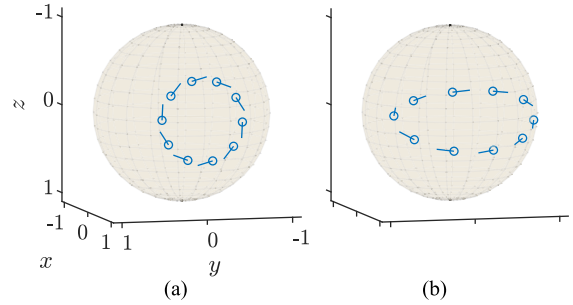


Fig. 4. Optimal solution to (11) for (a) $k_b = 10$ and (b) two more repulsive planes are added at the top and bottom. The arrows of the particles represent the velocity.

$k_{b,2} = k_{b,3} = 2$. This case corresponds to the situation when the vertical movement of the observer is limited. For instance, quadrotors usually have better agility in horizontal directions than the vertical ones. The result reveals the best placement is in a curved ellipse on a sphere. To gain some quantitative insights, we compare the results of 1000 examples with the result of the proposed method. In each example, the observation particles are randomly placed on the sphere but satisfy the constraints. The objective function values $\|G\|_F$ of the 1000 random examples are shown in Fig. 5, where the red line with $\|G\|_F = 5.93$ corresponds to the optimized placement in Fig. 3(d). The results show that all the objective function values for random placements are greater and hence worse than the result given by the proposed method.

In summary, the numerical solution to (11) suggests that a circular or elliptical movement of the observer will achieve the best observability of the target. This lays a theoretical foundation for us to design new observability-enhanced guidance laws in the next section. Moreover, compared to the recent works in [18]

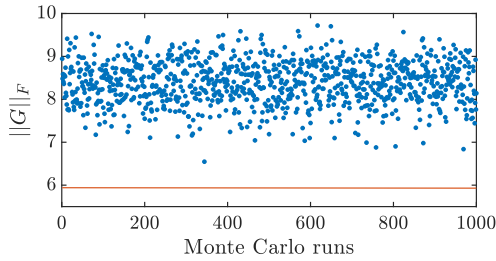


Fig. 5. Result of Monte Carlo simulations for 1000 times. The red line shows the $\|G\|_F$ of Fig. 3(d).

and [20], we have extended the analysis to 3-D and a multistep horizon case.

VI. 3-D HELICAL GUIDANCE LAW

In this section, we propose a novel observability-enhanced 3-D guidance law based on the theoretical results presented in Section V. Let $a_d \in \mathbb{R}^3$ be the desired acceleration of the pursuer. The proposed guidance law is

$$a_d = a_{HN} + a_{RC}. \quad (13)$$

The first term $a_{HN} \in \mathbb{R}^3$ is the lateral acceleration designed to enhance the observability. Under a_{HN} , the pursuer would fly along a helical curve, and hence, it is named *helical navigation guidance* (HNG). The second term $a_{RC} \in \mathbb{R}^3$ is the longitudinal acceleration designed to control the pursuer–target distance. It is notable that a_{HN} is always orthogonal to a_{RC} . The details are given as follows.

A. Helical Navigation Term

Although we have revealed in Section V that the pursuer moving along an ellipse on a sphere centered at the target would optimize the observability, the algorithm designed in Section V is not an implementable guidance law because the algorithm is to solve the optimization problem in (11) numerically but not the guidance problem. We design a new guidance law to realize the behavior suggested by the theoretical analysis. Moreover, when the target moves, moving on a sphere centered at the target would become a helical movement. Therefore, we design the following guidance law to achieve such helical behavior:

$$a_{HN} = Nv \times R_\eta R_Z R_Y e_X \times \lambda \quad (14)$$

where $N \in \mathbb{R}^+$ is the navigation gain, $v \in \mathbb{R}^3$ is the pursuer velocity, $\lambda \in \mathbb{R}^3$ is the LOS unit vector, and \times is the cross-product. The rotation matrices R_η , R_Z , and R_Y are defined as

$$\begin{aligned} R_\eta &= R_\eta(\theta_\eta) \\ R_Z &= R_Z(c_Z \sin(t)/\hat{r}) \\ R_Y &= R_Y(c_Y \cos(t)/\hat{r}) \end{aligned}$$

where $\eta = e_X \times \lambda$, $\theta_\eta = \cos^{-1}(\lambda^T e_X)$, $e_X = [1, 0, 0]^T$, and $c_Z, c_Y \in \mathbb{R}^+$ are the control gains. The matrices $R_Z(\alpha), R_Y(\alpha) \in SO(3)$ denote rotations about z, y -axis by angle α , respectively. The usage of $R_Z, R_Y \in \mathbb{R}^{3 \times 3}$ is to

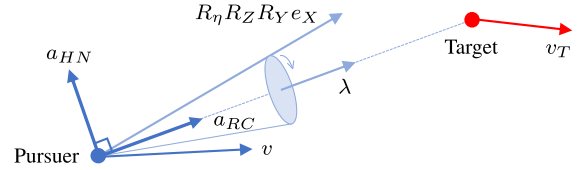


Fig. 6. Graphical illustration of the guidance law.

periodically change the directions of λ . The matrix $R_\eta(\theta_\eta)$ can be calculated by using the Rodrigues' rotation formula as $R_\eta(\theta_\eta) = I_{3 \times 3} + \sin \theta_\eta [\eta]_\times + (1 - \cos \theta_\eta) [\eta]_\times^2$, where $[\cdot]_\times : \mathbb{R}^3 \rightarrow \mathbb{R}^{3 \times 3}$ yields a skew symmetric matrix satisfying $[x]_\times y = x \times y$ for any $x, y \in \mathbb{R}^3$. A graphical illustration of the components of the HNG is shown in Fig. 6.

Some important and interesting properties of HNG are discussed below.

1) The guidance law would generate a weaving maneuver so that the trajectory of the pursuer is like a helical curve. It is notable that the weaving maneuver is relatively weak (i.e., the lateral acceleration perpendicular to the LOS is small) when the target range is large, and becomes stronger when the target range decreases. This is manifested by the division by \hat{r} in the expression of R_Z or R_Y . As a result, when the target range is large, HNG leads to a tail-chasing behavior, which is desired because the primary goal in this stage is to approach the target as fast as possible. Tail chasing is also beneficial for following maneuverable targets because the pursuer is unlikely to be thrown off by erratic maneuvers of targets as observed in the hunting behaviors of Hawks [53]. When the target range is small, the guidance law leads to a strong 3-D helical movement, which is also desired because the primary goal in this stage is to enhance the observability and hence estimate and control the target range accurately. Thus, tail chasing and helical following could be realized in a unified way by HNG.

2) One may wonder what happens when $\hat{r} = 0$. In fact, the division by \hat{r} in R_Z and R_Y could be removed (or equivalently setting $\hat{r} \equiv 1$). In this case, the observer is then purely dependent on λ . Although it does not require range estimation anymore, the cost is that the well-blended behavior of tail chasing and helical following disappears, because the guidance law always assumes that $\hat{r} = 1$. Therefore, if \hat{r} is trustable (not necessarily accurate), it could be used to better adjust the guidance behavior.

3) We can control the shape of the trajectory and hence the degree of observability enhancement by tuning c_Z and c_Y . In particular, large values of c_Z and c_Y would result in big ellipses and hence strong vehicle maneuvers. Small values will result in less maneuvers. In the extreme case of $c_Z = 0$ or $c_Y = 0$, the 3-D helical guidance will downgrade to planar weaving guidance. When $c_Z = c_Y = 0$, the helical guidance degenerates to pure PPG. As a result, PPG can be considered as a special case of HNG.

B. Range Control Term

Before presenting the proposed range controller, we define a few variables. While p_T and v_T are the position and velocity

of the target as defined in Section IV, we denote \hat{p}_T and \hat{v}_T as their estimates. Let $\Delta\hat{p} = \hat{p}_T - p \in \mathbb{R}^3$ and $\Delta\hat{v} = \hat{v}_T - v \in \mathbb{R}^3$. Suppose $r_d > 0 \in \mathbb{R}$ is the desired range. Then, the error between the estimated range and the desired one is defined as

$$\xi_1 = \|\Delta\hat{p}\| - r_d. \quad (15)$$

The time derivative of ξ_1 , or the range error rate, can be obtained as

$$\dot{\xi}_1 = \dot{\xi}_1 = \Delta\hat{p}^T \Delta\hat{v} / \|\Delta\hat{p}\|. \quad (16)$$

Define a virtual control variable v^* as

$$v^* = -k[\sigma(\xi_1) + \xi_2] - \sigma(\xi_1) - \sigma'(\xi_1)\xi_2 \quad (17)$$

where $k \in \mathbb{R}^+$ is the control gain and $\sigma(\cdot)$ is a well-defined saturation function that has finite first derivatives $\sigma'(x)$ with respect to x and $\sigma(0) = 0$. In this article, the saturation function is $\sigma(x) = 3 \tan^{-1}(x/3)$, which is selected based on the physical constraints of the quadrotor, and it is validated by real experiments in Section IX. More general saturation functions may also be applied [54].

We propose the following range controller:

$$a_{RC} = \frac{u^*}{\lambda^T \Delta\hat{p}} \lambda \quad (18)$$

where

$$u^* = -\|\Delta\hat{p}\|v^* + \Delta\hat{v}^T \Delta\hat{v} - \xi_2^2 - \Delta\hat{p}^T a_{HN} \quad (19)$$

in which v^* is defined in (17) and a_{HN} in (14).

Next, we show that the proposed range controller renders the range error ξ_1 convergent to zero asymptotically; thus, a desired range between the target and pursuer is reached. To do that, we assume that the target acceleration is zero, that is, $\dot{v}_T = 0$. This assumption is reasonable because target acceleration is not known. Then, substituting (18) into the error dynamics of ξ_1, ξ_2 defined in (15) and (16) gives the following closed-loop system dynamics:

$$\begin{aligned} \dot{\xi}_1 &= \xi_2 \\ \dot{\xi}_2 &= (\Delta\hat{v}^T \Delta\hat{v} - \xi_2^2 - \Delta\hat{p}^T \dot{v}) / \|\Delta\hat{p}\| = v^* \end{aligned}$$

where we used (13) and the fact that $\dot{v} = a_d$. Construct the Lyapunov function V as

$$V = \int_0^{\xi_1} \sigma(\tau) d\tau + \frac{1}{2}[\sigma(\xi_1) + \xi_2]^2.$$

Due to the property of the saturation function $\sigma(\cdot)$, the integral in V is positive definite, so as V . Taking the time derivative of V and substituting (17) yield

$$\dot{V} = -\sigma^2(\xi_1) - k[\sigma(\xi_1) + \xi_2]^2 < 0.$$

Moreover, since $\|\xi\| \rightarrow \infty$ implies the unboundedness of V , the origin of the closed-loop system is globally asymptotically stable according to the Lyapunov stability theorem [52].

Several remarks about the range controller are as follows.

1) The term $\Delta\hat{p}^T a_{HN}$ in (19) would vanish when the bearing measurement is accurate. In particular, when $\Delta\hat{p} / \|\Delta\hat{p}\| \approx \lambda$, we have $\Delta\hat{p}^T a_{HN} \approx 0$.

2) Even if the pursuer is far away from the target initially, the control command given by (18) would not be extremely large due to the saturation function in (17).

3) In theory, it is possible that $\lambda^T \Delta\hat{p} = 0$ in (18), especially when the initial estimate of \hat{p}_T is inaccurate. However, this problem can be easily avoided by selecting the initial value of \hat{p}_T to be consistent with $\tilde{\lambda}$. In fact, it is required to do so to ensure a reasonable initialization. In particular, although the range to the target is not known, the bearing vector $\tilde{\lambda}$ of the target is known (though with noise). Therefore, the initial guess of the target position should lie on the line along the bearing vector. In this case, the initial guess can be expressed as $\hat{p}_T(0) = p(0) + \hat{r}(0)\tilde{\lambda}(0)$, where $\hat{r}(0)$ is an initial guess of the target range. It follows that $\Delta\hat{p}(0) = \hat{r}(0)\tilde{\lambda}(0)$, and hence, $\tilde{\lambda}^T(0)\Delta\hat{p}(0) = \hat{r}(0)$, which is not zero as long as the initial guess of r is not zero.

4) The proposed range controller is not the only choice in controlling the range and it can be replaced by others. However, compared to a fine-tuned saturated proportional-derivative (PD) controller, simulation results show that the proposed method has better performance in the perspectives of accuracy and convergence speed due to the consideration of the nonlinear terms and the property of the saturation function.

VII. QUADROTOR CONTROLLER

In this section, we propose a low-level flight controller for the pursuer quadrotor to achieve the desired acceleration command given in (13). The design procedure follows the classic geometric control approach [55]. One different feature of the controller compared to conventional ones is that it enables the heading of the quadrotor (and hence the camera) to be always aligned with the target. Next, we present a concise derivation of it.

The dynamical model of a quadrotor is

$$\dot{p} = v \quad (20a)$$

$$\dot{v} = ge_Z - T/mRe_Z \quad (20b)$$

$$\dot{R} = R[\omega]_{\times} \quad (20c)$$

$$\dot{\omega} = -J^{-1}[\omega]_{\times} J\omega + J^{-1}\tau \quad (20d)$$

where $p, v, \omega \in \mathbb{R}^3$ are the position, velocity, and angular velocity of the quadrotor, respectively. The attitude is represented by the rotation matrix $R = [r_1, r_2, r_3] \in SO(3)$. The control inputs are $T \in \mathbb{R}^+$ and $\tau \in \mathbb{R}^3$, which are the total thrust and torque, respectively. In addition, m is the mass of the quadrotor, $J \in \mathbb{R}^{3 \times 3}$ is the moment of inertia, g is the gravitational constant, and $e_Z = [0, 0, 1]^T$. It is remarked that the body frame of the quadrotor is assumed to be forward-right-down; thus a minus sign is added before the thrust T in (20b).

Our objective is to design the thrust T and torque τ , through which we can easily compute the rotor speed using a linear mapping [56], which is our ultimate goal. To do that, let the right-hand side of (20b) be equal to a_d :

$$ge_Z - T/mRe_Z = a_d \quad (21)$$

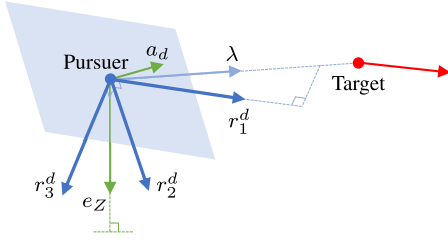


Fig. 7. Illustration of the components of the desired rotation matrix R_d .

which leads to $T/mRe_Z = ge_Z - a_d$. Then, the desired thrust direction can be calculated as

$$r_3^d = (ge_Z - a_d) / (\|ge_Z - a_d\|).$$

Since the heading of the quadrotor must be aligned with the target, the desired r_2 is designed as $r_2^d = r_3^d \times \lambda$. Consequently, the desired r_1 has to be $r_1^d = r_2^d \times r_3^d$, and hence, the complete desired rotation matrix is

$$R_d = [r_3^d \times \lambda \times r_3^d, r_3^d \times \lambda, r_3^d].$$

A graphical illustration of the columns of the desired rotation matrix R_d is shown in Fig. 7.

By multiplying by $e_Z^T R_d^T$ on both sides of (20b), the thrust command can be computed as

$$T = me_Z^T R_d^T (ge_Z - a_d). \quad (22)$$

To track the desired attitude R_d , we first define the tracking error as $e_R = \frac{1}{2}(R^T R_d - R_d^T R)^\vee$, where $\vee : \mathfrak{so}(3) \rightarrow \mathbb{R}^3$ is the inverse operator of $[\cdot]_\times$. The angular velocity error e_ω could be derived as $e_\omega = \omega - R_d^T R \omega_d$, where ω_d is the desired angular velocity. The time derivative of e_ω is

$$\dot{e}_\omega = \dot{\omega} + [\omega]_\times R^T R_d \omega_d - R^T R_d \dot{\omega}_d. \quad (23)$$

Substituting the rotation dynamics in (20d) into (23), a PD controller on the tangent bundle of $SO(3)$ can be defined as

$$\begin{aligned} \tau = & -k_p e_R - k_d e_\omega + [\omega]_\times J \omega \\ & - J ([\omega]_\times R^T R_d \omega_d - R^T R_d \dot{\omega}_d) \end{aligned} \quad (24)$$

where $k_p \in \mathbb{R}^+$ and $k_d \in \mathbb{R}^+$ are PD gains. In practice, the value of ω_d in (24) is usually set to be zero.

VIII. NUMERICAL SIMULATION

This section presents a set of simulation examples to demonstrate the proposed results. In particular, the simulation results verify the following:

- 1) the effectiveness of the proposed overall system to follow constant-velocity and maneuvering targets;
- 2) the superior performance of the proposed bearing-only estimator compared with other classic and state-of-the-art estimators;
- 3) the superior performance of the proposed HNG compared with other classic and state-of-the-art observability-enhanced guidance laws;
- 4) how the parameters in HNG impact the guidance performance.

TABLE I
PARAMETERS IN SIMULATION

Parameter	Variable	Value	Unit
Mass	m	1.5	kg
Gravitational acc.	g	9.81	m/s ²
Inertia in x, y-axis	J_{xx}, J_{yy}	1.745×10^{-2}	kg·m ²
Inertia in z-axis	J_{zz}	3.175×10^{-2}	kg·m ²
Arm length	d_{arm}	0.225	m
Propeller thrust coef.	C_T	1.105×10^{-5}	N/(rad/s) ²
Propeller moment coef.	C_m	1.489×10^{-7}	N·m/(rad/s) ²
Motor response time	T_m	0.0136	s
Air-drag coefficient	C_d	6.579×10^{-2}	N/(m/s) ²
Focal length	f	0.008	m
Pixel size	ρ_w, ρ_h	10^{-5}	m
Principle point	u_0, v_0	512	pixel

To make the simulation environment realistic, the following points are considered.

1) Electric motor hysteresis is considered and modeled by a first-order transfer function as $1/(T_m s + 1)$, where T_m is a time constant as shown in Table I.

2) The thrust for each rotor is saturated and the total thrust cannot exceed 1.5 times the gravity.

3) Drag, mainly coming from the blade flapping and the induced drag associated with rigidity of the blade, is modified from an effective lumped parameter model in [57] as $-K_r R^T v$, where $K_r = \text{diag}(C_d, C_d, 0)$ and C_d is a linear drag coefficient.

4) Noise is added to the feedback of quadrotor's velocity and position as $\sigma_v \sim \mathcal{N}(0, 0.05)$ and $\sigma_p \sim \mathcal{N}(0, 0.1)$, respectively.

In all the simulation examples in this article, we deliberately keep all the parameters in the proposed algorithms the same to verify the robustness of the algorithm across different scenarios. The parameters used are summarized in Table I. Better performances could be achieved for any specific scenarios with fine-tuned parameter values.

In the simulation, the vision system, target state observer, guidance, and flight control modules are all incorporated. In the vision system, a pin-hole camera model is established for perceiving the target whose pixel coordinate is then transformed to an LOS vector in the navigation frame. The overall control architecture is as shown in Fig. 2.

A. Effectiveness of the Overall System

Next, we show examples to demonstrate the effectiveness of the overall system.

1) *Constant-Velocity Target*: In this example, the quadrotor is commanded to follow a constant-velocity target $v_T = [3, 4, 0]^T$ m/s starting from the initial position $p_T(0) = [50, -25, -20]^T$ m. The quadrotor should be eventually keep a desired distance $r_d = 8$ m apart from the target. The initial position and velocity of the quadrotor are $[0, 0, 0]^T$ m and $[2, 0, 0]^T$ m/s, respectively. The initial target estimate is $\hat{p}_T = [40, -20, -15]^T$ m and $\hat{v}_T = [0, 0, 0]^T$ m/s. The covariance of process noise of the target is $Q = 0.04I_{3 \times 3}$ and the covariance of measurement noise is $\Sigma = 10^{-4}I_{3 \times 3}$. The HNG gains in (14) are $N = 3$ and $c_Z = c_Y = 3.5$.

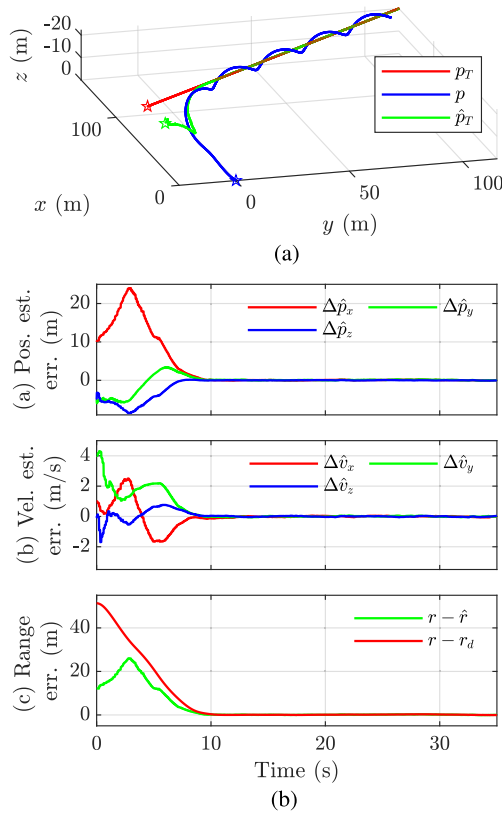


Fig. 8. Simulation results of the overall system against a constant-velocity target. The symbol \star represents starting positions.

The trajectories of the target, estimated target, and pursuer are shown in Fig. 8(a). As can be seen, the quadrotor approaches the target with a flat trajectory and then follows the target with a helical trajectory. The estimation errors of the target position, velocity, and range are shown in Fig. 8(b). As can be seen, the errors converge to zero quickly.

2) *Varying-Velocity Target*: Although the proposed algorithms are designed for constant-velocity targets, they could also handle maneuvering targets to a certain extent thanks to the observability enhancing strategy. In this example, all the parameters are the same as the previous constant-velocity example, except that a lateral acceleration with a magnitude of 0.5 m/s^2 is applied to the normal of the target velocity from 0 to 20 s. Then, it turns left with the opposite acceleration direction from 20 to 30 s so that it shows an “s” maneuver.

The trajectories are shown in Fig. 9(a). Similarly, the trajectory of the approaching stage is relatively flat and the trajectory of the following stage presents a helical shape. The estimation errors are shown in Fig. 9(b). As can be seen, the estimation errors do not converge to zero, which is not surprising because the acceleration of the target is not known or estimated by the pursuer. Nevertheless, the quadrotor could still successfully estimate and follow the target with a low estimation error.

B. Comparison With Other Bearing-Only Observers

Next, we compare the performance of the proposed u-PLKF with other algorithms including the classic EKF, the optimal

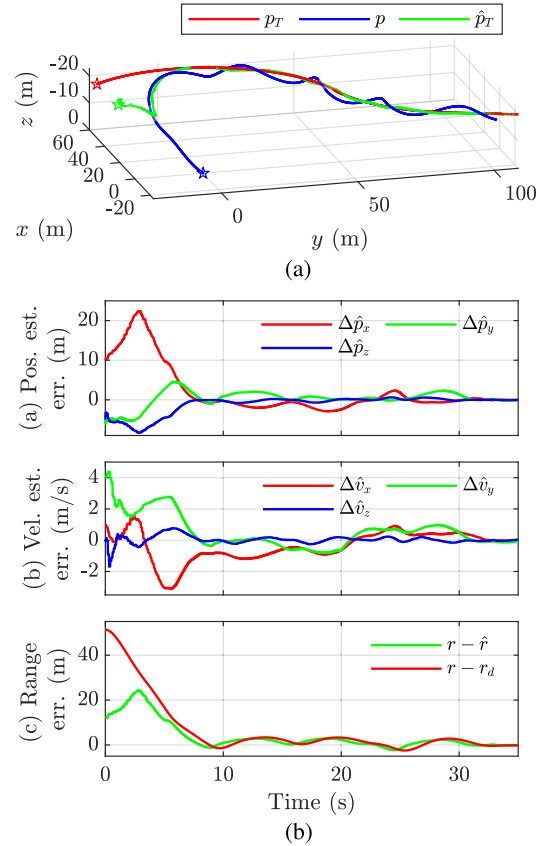


Fig. 9. Simulation results of the overall system against a varying-velocity target. The symbol \star represents starting positions.

u-PLKF, and a state-of-the-art one proposed in [29]. Here, in the classic EKF, the measurement is selected as the azimuth and elevation angle of LOS. The optimal u-PLKF is a version of u-PLKF where the measurement matrix in (6) is intentionally set to be noise-free. It serves as a performance baseline to evaluate its effectiveness as a latent variable observer, and will not be used in practice. The introduction of the optimal u-PLKF is inspired by [29]. The state-of-the-art one in [29] is a kind of PLKF where some techniques are used to compensate for bias but as usual, a two-angle representation is used.

Instead of comparing the four algorithms using one single example, we conduct a total of 100 Monte Carlo runs to examine their performances. In each Monte Carlo run, the target estimate \hat{p}_T is firstly uniformly drawn from $[20, 120] \text{ m}$, $[-50, 50] \text{ m}$, and $[-50, 50] \text{ m}$ for x , y , and z directions, respectively. Then, with the same initialization, each quadrotor equipped with one kind of estimator, is commanded to track a constant moving target as shown in Section VIII-A. This process is repeated for 100 times.

The average range errors by the four estimators are shown in Fig. 10. As can be seen, the EKF method suffers from a severe instability problem when the initialization error is large. As a comparison, the proposed u-PLKF retains its stability even with large initialization errors. The accuracy of u-PLKF is also better than the 3-D bias-compensation pseudomeasurement Kalman filter proposed in [29]. Moreover, the expression and implementation of u-PLKF are much simpler than the one

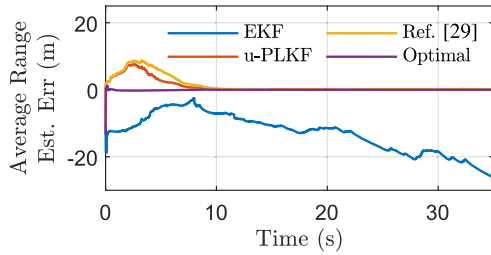


Fig. 10. Average range estimation errors using four different observers: EKF, u-PLKF, observer in [29] and optimal u-PLKF. A total of 100 Monte Carlo runs with various position estimation initializations have been considered.

in [29] where the measurements are represented by using two angles (azimuth and elevation), which results in the complicated computation of the covariance matrix of the noise (see [29, Appendix A]). Finally, the fast convergence of the optimal u-PLKF, as a benchmark, elucidates we can significantly reduce estimate errors by increasing measurement accuracy.

C. Comparison With Other Guidance Laws

Next, we show the superior performance of the proposed helical guidance law compared with other guidance or control laws. It is notable that there does not exist any guidance or control law that could be directly applied to solve the task studied in this article. Nevertheless, we believe that it is still meaningful to compare with some representative guidance laws by slightly modifying them. In particular, we select two classes of guidance/control laws to compare. The first class is the classic PNG, PPG, and PD control, which does not take the observability enhancement into consideration particularly. The second class is the state-of-the-art observability-enhanced bearing-only guidance laws [14], [58]. Since these guidance laws may not be applicable to 3-D cases or could not control the target range, we adapt them to a certain extent so that they could be incorporated into our control framework. Details are given below.

1) *Classic Guidance and Control Laws:* Next, we compare HNG with PNG, PPG, and PD control. In the PPG case, the aerial vehicle is steered so that its velocity vector points to the target. To achieve this kind of motion in 3-D and meanwhile fit for the control architecture where the lateral acceleration is designed to be perpendicular to the LOS, we design the following PPG law tailored from the classic one in [34]: $a = N(v \times \lambda) \times \lambda$, where $v \in \mathbb{R}^3$ is the velocity, $\lambda \in \mathbb{R}^3$ is again the LOS unit vector, and $N \in \mathbb{R}^+$ is the gain. The range controlling term is the same as in (18). In the PD control case, the overall acceleration is $a = k_P(p_d - p) + k_D(\dot{v}_T - v)$, where $p_d = \hat{p}_T - r_d\lambda$, $k_P = 0.5$, and $k_D = 0.2$. The rest of the control architecture is the same as the HNG case, as shown in Fig. 2.

The resulting trajectories using PNG, PPG, and PD control are shown in Fig. 11. All of them fail to follow the target satisfactorily even if the target moves with a constant velocity. The reason for the failure lies in the characteristics of those guidance laws, that is, the lack of observability enhancement. Thus, these results verify the necessity of observability-enhancing maneuvers.

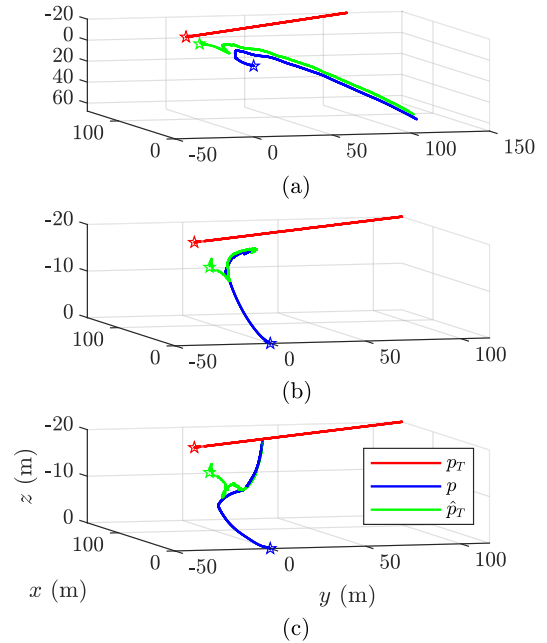


Fig. 11. Trajectories for following a constant moving target using (a) PNG, (b) PPG, and (c) PD controller, respectively. The symbol \star represents starting positions.

2) *State-of-the-Art Observability-Enhanced Guidance Laws:* Next, we compare HNG with two recent observability-enhanced guidance laws. The first one is derived in both [14] and [16] and the second in [43]. The two guidance laws are designed for target interception instead of target following. In order to compare with HNG, we embed the guidance laws into the control architecture, as shown in Fig. 2. The embedding is achieved by replacing the HNG command in (14). Since the guidance law in [14] and [16] is designed for the 2-D case, we compute the control commands in the horizontal and vertical plane separately first and then combine them together. Moreover, the constant speed assumption in [14] and [16] is ignored since the speed must be varying in our target tracking task.

Details of the two observability-enhanced guidance laws and their performance are given below.

First, the authors of [14] and [16] use the lower bound of the determinant of FIM to derive an optimal guidance law. The performance index is proportional to the bearing rate and inversely proportional to the square of the range. The derivation process of the expressions of the states and costates defined in [14] and [16] are intricate. However, the final optimal solution is simple, and the corresponding acceleration command can be computed as $a = -2||v||\dot{\theta}$, where $\dot{\theta}$ is the bearing rate in 2-D. Surprisingly, this can be considered as a *retro-PNG*.

The overall performance is acceptable for tracking a constant moving target; however, it fails for a maneuvering target as shown in Fig. 12(a). The failure is mainly caused by the lack of observability of retro-PNG in the latter following stage letting the LOS rate tend to zero.

In [43], the authors use the zero-effort-miss (ZEM) z to formulate an indefinite linear-quadratic optimization problem. The ZEM is defined as the distance that the missile would miss if

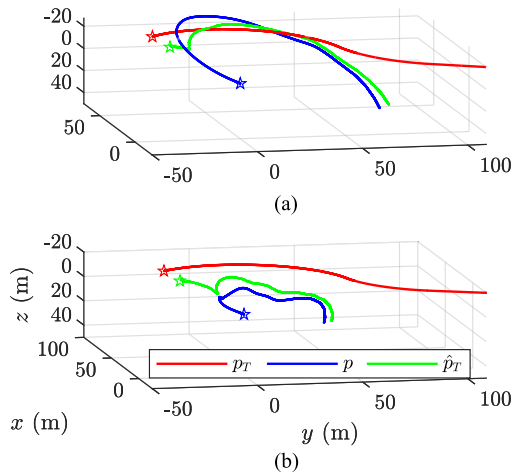


Fig. 12. Trajectories for following a *maneuvering* target using (a) retro-PNG derived in [14] and [16], and (b) linear observability-enhancement guidance law proposed in [43]. The symbol \star represents starting positions.

the missile does not make any further corrective maneuvers and maintains its current course. The optimal guidance command is finally obtained as

$$a = k_w t_{go} z \cot(k_w t_{go}^3 / 3)$$

where $t_{go} \in \mathbb{R}$ is time-to-go and $k_w \in \mathbb{R}^+$ is a designing parameter. By defining $N = k_w t_{go}^3 \cot(k_w t_{go}^3 / 3)$, the command is rewritten as $a = N v_c \dot{\theta}$, where $v_c \in \mathbb{R}$ is the closing speed and $\dot{\theta} \in \mathbb{R}$ is the bearing rate. The design criterion for choosing k_w is to let $\pi/2 < k_w t_{go}^3 / 3 < \pi$ to ensure bounded optimal solution [43]. Under this condition, the navigation gain $k_w t_{go}^3 \cot(k_w t_{go}^3 / 3)$ will gradually increase from negative to positive values, indicating a switch from retro-PNG to classic PNG.

The performance for tracking a constant moving target is acceptable but not for maneuvering targets, as shown in Fig. 12(b). The failure is mainly caused by the following two reasons. First, this method relies on an accurate estimation of time-to-go. If the estimated time-to-go is not accurate enough, it will generate an unexpected oscillation command which tends to infinity caused by the periodic properties of cotangent functions. Second, the guidance law in [43] is designed for target interception task but not for target following. The definition of the time-to-go in the target following task actually cannot be accurately defined causing the optimal guidance law in [43] not to function well.

D. Tuning Parameters in Helical Guidance Law

Next, we study the impacts of the parameters of HNG on the target following performance.

We evaluate the guidance performance using four sets of parameters as shown in Table II. Note that the parameters in set d) are those used in Section VIII-A. The simulation setup is the same as in Section VIII-A.

The range estimate errors for the four cases are shown in Fig. 13. By comparing Fig. 13(a) and (b), we know that increasing N could improve the accuracy of range estimation. This is

TABLE II
TUNING PARAMETERS IN HELICAL GUIDANCE LAW

Parameter	N	c_Z	c_Y
a)	1	3	3
b)	3	3	3
c)	3	3	0
d)	3	3.5	3.5

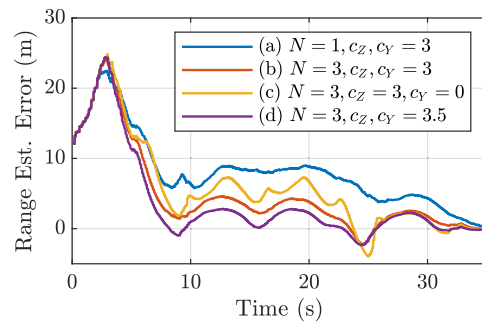


Fig. 13. Range estimation errors in tracking a maneuvering target using four different sets of parameters for the HNG.

because larger N will result in a larger acceleration and thus a stronger maneuver of the observer. A similar finding could be obtained when we compare Fig. 13(b) and (d): larger values of c_Z and c_Y will force the quadrotor to weave in a larger magnitude within the same time period and hence stronger maneuver. Finally, when $c_Y = 0$, the observer merely maneuvers in a plane. In this case, the range estimation error becomes larger, verifying the benefits of exploiting the higher DOF in 3-D.

Although increasing N , c_Z , and c_Y will enhance the maneuverability of the observer and thereby improve the observability of the target, there are several constraints for doing that. For example, the quadrotor has a limit of maneuverability due to dynamic constraints. Moreover, the excessive maneuver may cause the quadrotor to lose sight of the target given of limited field of view (FoV) of the camera. To see this, consider the image point of the target in a vertical normalized image plane sharing the same position and yaw angle with the quadrotor. The image points are obtained by using the pin-hole camera model [9].

The image trajectories for the four cases are shown in Fig. 14. It is noticed that increasing the values of N , c_Z , and c_Y will expand the moving area of the image point, meaning that it would be harder for the target point to remain inside the FoV. Although such a problem may be eased by using a pan-tilt camera, the pan-tilt mechanism still has a rotational limit. In summary, these constraints should be considered when designing the desired helical maneuver of the observer.

IX. EXPERIMENTAL VALIDATION

In this section, we present real flight experimental results to show the effectiveness and robustness of the proposed approaches.

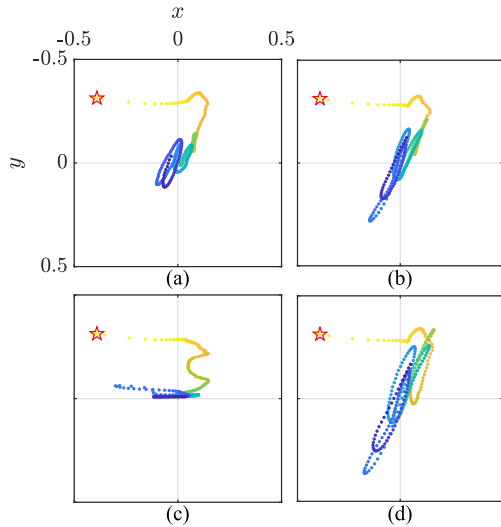


Fig. 14. Trajectories of the maneuvering target in the normalized image plane for the four sets of parameters. The symbol \star means the starting points.

TABLE III
KEY SPECIFICATIONS OF DJI M300

Parameter	Value	Unit
Dimension	$810 \times 670 \times 430$	mm
Motor-to-motor	895	mm
Mass	6.3	kg
Max takeoff weight	9	kg
Max pitch/roll	30	degree
Duration (nominal)	55	min

A. Experiment Setup

We built up the system based on two DJI M300 quadrotor platforms. The key specification of the quadrotor is reported in Table III. To deploy the proposed algorithms, we installed an extra onboard computer Manifold2, as shown in Fig. 15(a), and a pair of Zigbee modules for wireless communication. The hardware setup for the target MAV is the same as the pursuer MAV.

As aforementioned, we do not consider visual detection of MAVs in this article, because it is nontrivial and will be addressed specifically in other works of ours in the future. In our experiments, the target position is transmitted to the pursuer based on wireless communication. Then, the bearing of the target is reconstructed based on the transmitted target position. It should be noted that the pursuer MAV *only* utilizes the bearing information of the target.

The overall communication structure for the demonstration prototype is illustrated in Fig. 16. We set up two Zigbee mesh networks, namely network A and network B with two independent channels. In network A, Zigbee A3 is used to send the action/abort commands to the target MAV. Zigbee A1 is used to send the target position from the global positioning system to Zigbee A2. In network B, Zigbee B1 sends the target estimate and pursuer state to B2, and B2 is used to send action/abort command to the pursuer MAV.

The estimator/guidance module in Fig. 16 is deployed on the Manifold2 onboard computer, and embedded in a robotic operating system network. It sends control commands to the software development kit (SDK) of DJI M300 and meanwhile receives the flight states from the SDK. The estimator is the u-PLKF detailed in Section IV, and the guidance law is as shown in Section VI. To fit for the onboard SDK of DJI, the acceleration command computed from the guidance law (13) is directly mapped to the thrust and attitude command according to (20b), which is then fed to the SDK. It is remarked that the estimator designed based on the discrete-time double-integrator model and the controller designed based on the continuous-time nonlinear model are compatible in real implementation. That is because the estimator and controller are two separate components. The controller only needs to receive the output of the estimator at a certain frequency. In our implementation, the estimator outputs the state estimate of the target at 50 Hz, whereas the controller is implemented at 20 Hz. The measurement frequency is set as 5 Hz, which is intentionally tuned low considering that the update rate of onboard vision systems is generally low.

The procedure of the experiment is as follows. The target MAV is first commanded to fly with constant or varying-velocity in the air [see the trajectories in Figs. 17(a) and 18(a)]. The pursuer MAV is then commanded to take off and ascend to a specified height in order to avoid trees and buildings. After it reaches a specified height, the estimation, guidance, and control modules are activated automatically.

We conducted more than 30 test flights for tracking different constant-velocity and varying-velocity targets, and Fig. 15 shows the scenarios of these tests. Only two test flights fail the target following mission. The failure was caused by the interruption of Zigbee signals, which could be alleviated by replacing them with more reliable ones. In addition, the updating rates of the controller and estimator should be carefully selected considering the hardware performance, especially the Zigbee modules.

B. Experimental Results

1) *Constant-Velocity Target*: In this experiment, the pursuer MAV aims to follow a target with a constant velocity of $v_T = [4, 3, 0]^T$ m/s. The desired distance is set as $r_d = 15$ m apart from the target. The initial target estimate is $\hat{p}_T = [40, 0, -30]^T$ m and $\hat{v}_T = [0, 0, 0]^T$ m/s. It is remarked that the proposed u-PLKF is quite robust to these initializations as verified in Section VIII-B; thus, the change of these initial values will not have a great influence on the convergence of estimate errors. The covariance of process noise of the target is set as $Q = 1.5I_{3 \times 3}$, and the covariance of measurement noise is $\Sigma = 10^{-4}I_{3 \times 3}$. The HNG gains in (14) are $N = 1$ and $c_Z = c_Y = 3.5$.

The trajectories of the target, estimated target, and pursuer are shown in Fig. 17(a). A long-exposure photo of the pursuer MAV following a constant-velocity target MAV is shown in Fig. 1. As anticipated, the quadrotor approaches the target with a relatively flat trajectory and then follows the target with a helical trajectory. The estimation errors of the target position, velocity, and range are shown in Fig. 17(b). As can be seen, the errors converge to

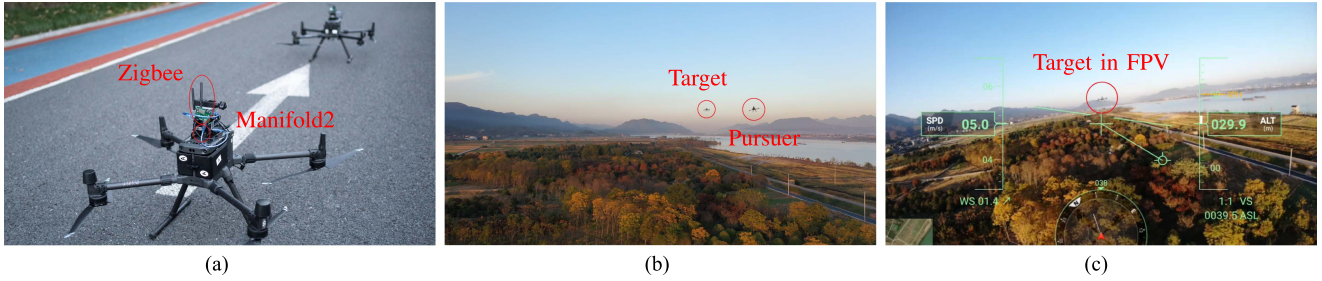


Fig. 15. (a) Customized pursuer and target MAV platforms. (b) A flight experimental scenario. (c) First-person-view (FPV) from the pursuer MAV.

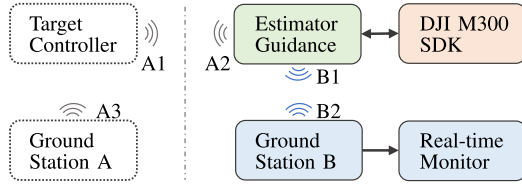


Fig. 16. Communication structure of the demonstration prototype.

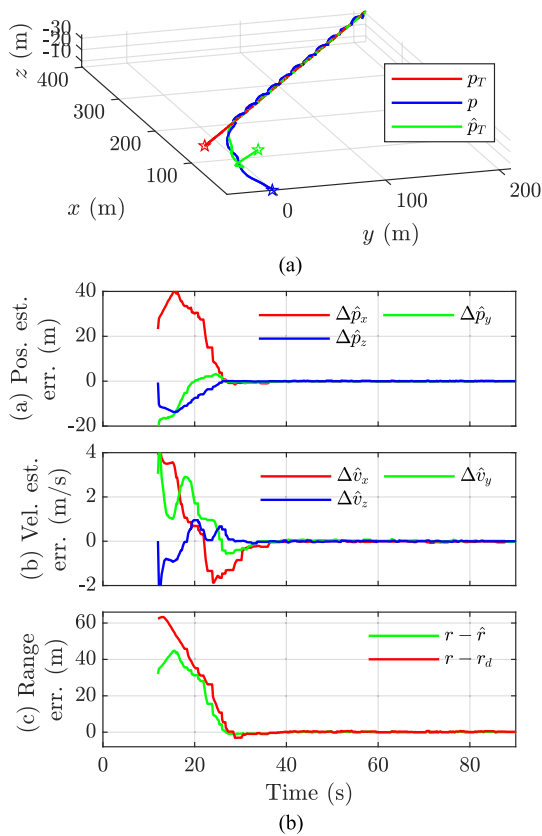


Fig. 17. Experimental results of following a constant-velocity target. The symbol \star represents starting positions.

zero quickly. Note since there is a takeoff and ascending process for the pursuer MAV, and the estimator does not start to work until some time before 20 s, during which the data are not shown in Fig. 17(b).

2) *Varying-Velocity Target*: In this demonstration, without tuning any parameters, the pursuer MAV is commanded to

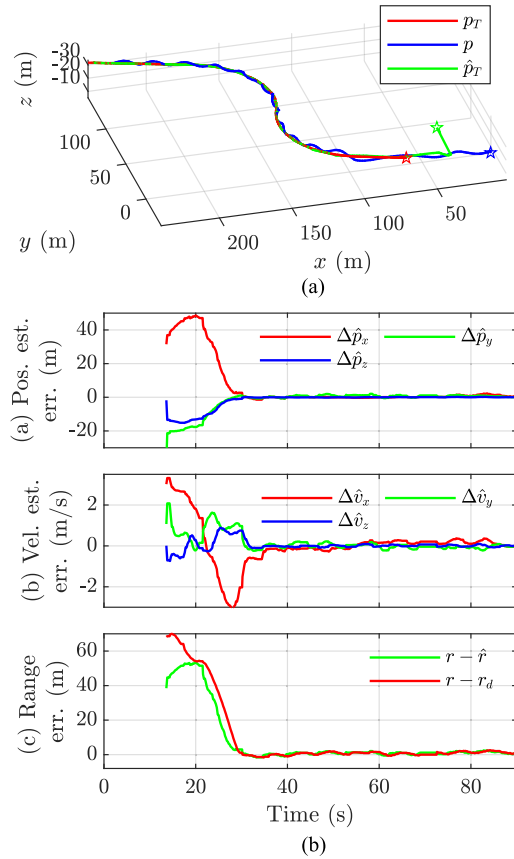


Fig. 18. Experimental results of following a varying-velocity target. The symbol \star represents starting positions.

follow a varying-velocity target which has an initial velocity of $[3, 1, 0]^T$ m/s. The target then makes a right turn of 90° in 30 s with the same velocity magnitude, and then makes an opposite maneuver. The lateral acceleration can be calculated as around 0.17 m/s^2 .

The trajectory is shown in Fig. 18(a) and the estimation errors are shown in Fig. 18(b). Similar to the simulation results in Fig. 9, although the estimation errors do not converge to zero, it is kept below 2 m for range estimate error in this demonstration.

X. CONCLUSION

This article has addressed the bearing-only target following problem in 3-D. The motivation is the application of defending

malicious MAVs when the target bearing can be measured by onboard visual sensors. First, we proposed a PLKF that has superior stability property and a concise form. It can be easily deployed on small onboard computers due to its simplicity and it is suitable for real-time applications. Second, we proposed a new perspective for observability analysis in bearing-only target estimation. The theoretical analysis can deepen our theoretical understanding of observability enhancement in 3-D. Third, we designed a 3-D helical guidance law that better exploits the additional freedom in 3-D to enhance observability. This guidance law has a simple structure and can be easily implemented on real systems. We also proposed a low-level flight controller incorporating the heading constraint based on geometric control which is beneficial to visual detection. Extensive numerical simulation results and comparisons with state-of-the-art approaches are presented. Finally, we have built a robust demonstration prototype that seamlessly integrates the algorithms and the communication with the MAVs. Experiments on real quadrotor platforms have been conducted to validate the effectiveness and robustness of the proposed approaches. This article only considers the one-to-one following. When multiple targets or pursuers are present, the problem becomes more complex. Therefore, a promising direction in the future is to consider cooperative estimation algorithms and cooperative guidance laws. In addition, the proposed approach is designed for constant-velocity or slight varying-velocity targets. How to handle highly maneuvering targets is also an important direction.

APPENDIX A

PRODUCTIVE MODEL OF LOS MEASUREMENT

We first present how (4) is obtained. In practice, we usually obtain a noise-corrupted bearing, denoted as $\tilde{\lambda}$, which is the product of a rotation matrix and λ :

$$\tilde{\lambda} = R_\eta(\epsilon)\lambda \quad (25)$$

where $R_\eta(\epsilon) \in \mathbb{R}^{3 \times 3}$ denotes a rotation about the η -axis by ϵ . Here, η is a unit vector and ϵ is a normally distributed measurement noise: $\epsilon \sim \mathcal{N}(0, \sigma_\epsilon^2)$. Equation (25) could be rewritten as $\tilde{\lambda} = \lambda + \nu$, where $\nu = (R_\eta(\epsilon) - I_{3 \times 3})\lambda$. Although ν depends on λ , it is a common operation to approximately assume ν to be normally distributed, as shown in (4). The main reason is the *additive* noise in (4) is easy to handle by Kalman filtering, whereas the *multiplicative* noise in (25) is not. This operation has been widely used and shows stable performance in gradient-based optimization [33] and bearing-only localization [59].

Next, we present the measurement equation and noise covariance matrix when the bearing is modeled in a multiplicative way as in (25). The purpose of showing this is twofold. First, the result of the multiplicative form may have potential applications in the future. Second, it serves as a comparison to highlight the simplicity of the proposed method. Denote an arbitrary unit vector perpendicular to λ as λ^\perp , and define a rotation axis $\eta = \lambda \times \lambda^\perp$. Using Rodrigues' rotation formula, $R_\eta(\epsilon)$ in (25) can be expressed as

$$R_\eta(\epsilon) = I_{3 \times 3} + \sin \epsilon [\eta]_\times + (1 - \cos \epsilon) [\eta]_\times^2$$

and the measurement model in (25) can then be rewritten as

$$\tilde{\lambda} = \lambda - \sin \epsilon \lambda^\perp + (1 - \cos \epsilon) \lambda. \quad (26)$$

Substituting (26) into (5), we have

$$P_\lambda = I_{3 \times 3} - \tilde{\lambda} \tilde{\lambda}^T$$

which can be reduced to

$$0 = P_\lambda (p_T - p) + \nu \quad (27)$$

where

$$\nu = r [(1 - \cos \epsilon)(3 - \cos \epsilon)\lambda - \sin \epsilon (2 - \cos \epsilon)\lambda^\perp] \quad (28)$$

is the new "transformed" measurement noise. In the derivation, the fact $P_\lambda (p_T - p) = r P_\lambda \lambda = 0$ is used and $r = \|p_T - p\|$ is the range between the target and observer. Now, (27) becomes our new measurement equation. Note that the ν in (27) is different from that in (4) or (6).

By inspecting (27) and (28), we conclude that the estimation accuracy of p_T is dependent on the range r and the covariance of ν is proportional to the square of the range. Specifically, by using small angle approximation of the noise ϵ , we can find the covariance matrix of the ν as

$$\Sigma_\nu = \frac{r_d^2 \sigma_\epsilon^2}{2} \text{diag} \left(\begin{bmatrix} \sin^2 \theta_\lambda \cos^2 \psi_\lambda + \sin^2 \psi_\lambda \\ \sin^2 \theta_\lambda \sin^2 \psi_\lambda + \cos^2 \psi_\lambda \\ \cos^2 \theta_\lambda \end{bmatrix} \right) + 3r_d^2 \sigma_\epsilon^4 \lambda \lambda^T \quad (29)$$

where $\theta_\lambda = \sin^{-1} \lambda_3$, $\psi_\lambda = \tan^{-1}(\lambda_2/\lambda_1)$, and $\lambda = [\lambda_1, \lambda_2, \lambda_3]^T$. From (29), we can infer that the covariance matrix Σ_ν is coupled with both the LOS unit vector λ and the range r .

Next, we derive the noise covariance in (29). Starting from the pseudomeasurement equation in (27), by using small angle approximation of ϵ , that is, $\sin \epsilon \approx \epsilon$ and $\cos \epsilon \approx 1 - \epsilon^2/2$, the covariance of ν can be obtained as

$$\mathbb{E}[\nu \nu^T] = r_d^2 \left(\mathbb{E}[\epsilon^4] \lambda \lambda^T - \mathbb{E}[\epsilon^3] \mathbb{E}[\lambda \lambda^{\perp T}] + \mathbb{E}[\epsilon^2] \mathbb{E}[\lambda^\perp \lambda^{\perp T}] \right).$$

With the assumption that the measurement noise is Gaussian distributed, that is, $\epsilon \sim \mathcal{N}(0, \sigma_\epsilon^2)$, we have $\mathbb{E}[\epsilon^4] = 3\sigma_\epsilon^4$, $\mathbb{E}[\epsilon^3] = 0$, and $\mathbb{E}[\epsilon^2] = \sigma_\epsilon^2$. The covariance matrix can then be reduced to

$$\mathbb{E}[\nu \nu^T] = r_d^2 \sigma_\epsilon^2 \left(3\sigma_\epsilon^2 \lambda \lambda^T + \mathbb{E}[\lambda^\perp \lambda^{\perp T}] \right).$$

To find the expression of $\mathbb{E}[\lambda^\perp \lambda^{\perp T}]$, we express λ as

$$\lambda = [\cos \theta \cos \psi, \cos \theta \sin \psi, \sin \theta]^T$$

then the arbitrary vector λ^\perp can be written as

$$\begin{aligned} \lambda^\perp &= R_z(\psi) R_y(\theta) R_x(\phi) [0, 1, 0]^T \\ &= \begin{bmatrix} \sin \phi \sin \theta \cos \psi - \cos \phi \sin \psi \\ \sin \phi \sin \theta \sin \psi - \cos \phi \cos \psi \\ \sin \phi \cos \theta \end{bmatrix} \end{aligned}$$

where ϕ is uniformly distributed in $[-\pi, \pi]$. Then,

$$\mathbb{E}[\lambda^\perp \lambda^{\perp T}] = (\sin^2 \theta \cos^2 \psi + \sin^2 \psi) / 2$$

$$\mathbb{E}[\lambda_2^2] = (\sin^2 \theta \sin^2 \psi + \cos^2 \psi)/2$$

$$\mathbb{E}[\lambda_3^2] = (\cos^2 \theta)/2$$

where the following facts are used: $\mathbb{E}[\sin^2 \phi] = \mathbb{E}[\cos^2 \phi] = 1/2$ and $\mathbb{E}[\sin \phi \cos \phi] = 0$. The covariance is finally obtained as in (29).

ACKNOWLEDGMENT

The authors would like to thank Huaben Chen for the help in the C++ interface with DJI SDK, and Fei Chen for the assistance in outdoor experiments.

REFERENCES

- [1] M. Bibuli, M. Caccia, L. Lapiere, and G. Bruzzone, "Guidance of unmanned surface vehicles: Experiments in vehicle following," *IEEE Robot. Autom. Mag.*, vol. 19, no. 3, pp. 92–102, Sep. 2012.
- [2] T. Oliveira, A. P. Aguiar, and P. Encarnacao, "Moving path following for unmanned aerial vehicles with applications to single and multiple target tracking problems," *IEEE Trans. Robot.*, vol. 32, no. 5, pp. 1062–1078, Oct. 2016.
- [3] M. Bhargavapuri, A. K. Shastri, H. Sinha, S. R. Sahoo, and M. Kothari, "Vision-based autonomous tracking and landing of a fully-actuated rotorcraft," *Control Eng. Pract.*, vol. 89, pp. 113–129, 2019.
- [4] F. Morbidi and G. L. Mariottini, "Active target tracking and cooperative localization for teams of aerial vehicles," *IEEE Trans. Control Syst. Technol.*, vol. 21, no. 5, pp. 1694–1707, Sep. 2013.
- [5] A. Franchi, P. Stegagno, and G. Oriolo, "Decentralized multi-robot encirclement of a 3D target with guaranteed collision avoidance," *Auton. Robots*, vol. 40, no. 2, pp. 245–265, 2016.
- [6] F. Lin, K. Peng, X. Dong, S. Zhao, and B. M. Chen, "Vision-based formation for UAVs," in *Proc. IEEE Int. Conf. Control Autom.*, 2014, pp. 1375–1380.
- [7] M. W. Ashraf, W. Sultani, and M. Shah, "Dogfight: Detecting drones from drones videos," in *Proc. IEEE/CVF Conf. Comput. Vis. Pattern Recognit.*, 2021, pp. 7067–7076.
- [8] Y. Zheng, Z. Chen, D. Lv, Z. Li, Z. Lan, and S. Zhao, "Air-to-air visual detection of micro-UAVs: An experimental evaluation of deep learning," *IEEE Robot. Autom. Lett.*, vol. 6, no. 2, pp. 1020–1027, Apr. 2021.
- [9] Y. Ma, S. Soatto, J. Košecák, and S. Sastry, *An Invitation to 3-D Vision: From Images to Geometric Models*, vol. 26. Berlin, Germany: Springer, 2004.
- [10] A. Rozantsev, V. Lepetit, and P. Fua, "Detecting flying objects using a single moving camera," *IEEE Trans. Pattern Anal. Mach. Intell.*, vol. 39, no. 5, pp. 879–892, May 2017.
- [11] M. Derome, A. Plyer, M. Sanfourche, and G. L. Besnerais, "Moving object detection in real-time using stereo from a mobile platform," *Unmanned Syst.*, vol. 3, no. 4, pp. 253–266, 2015.
- [12] H. Hoelzer, G. Johnson, and A. Cohen, "Modified polar coordinates—the key to well behaved bearings only ranging," IBM, Manassas, VA, USA, IR&D. Rep. 78–M19, 1978.
- [13] S. C. Nardone and V. J. Aidala, "Observability criteria for bearings-only target motion analysis," *IEEE Trans. Aerosp. Electron. Syst.*, vol. AES-17, no. 2, pp. 162–166, Mar. 1981.
- [14] J.-P. Le Cadre and S. Laurent-Michel, "Optimizing the receiver maneuvers for bearings-only tracking," *Automatica*, vol. 35, no. 4, pp. 591–606, 1999.
- [15] E. L. Lehmann and G. Casella, *Theory of Point Estimation*. Berlin, Germany: Springer Sci. Bus. Media, 2006.
- [16] S. Hammel, P. Liu, E. Hilliard, and K. Gong, "Optimal observer motion for localization with bearing measurements," *Comput. Math. Appl.*, vol. 18, no. 1/3, pp. 171–180, 1989.
- [17] M. Sabet, A. Fathi, and H. M. Daniali, "Optimal design of the own ship maneuver in the bearing-only target motion analysis problem using a heuristically supervised extended Kalman filter," *Ocean Eng.*, vol. 123, pp. 146–153, 2016.
- [18] P. Anjaly and A. Ratnoo, "Observability enhancement of maneuvering target with bearings-only information," *AIAA J. Guid., Control, Dyn.*, vol. 41, no. 1, pp. 184–198, 2018.
- [19] D. C. Woffinden and D. K. Geller, "Optimal orbital rendezvous maneuvering for angles-only navigation," *AIAA J. Guid. Control Dyn.*, vol. 32, no. 4, pp. 1382–1387, 2009.
- [20] S. He, H.-S. Shin, and A. Tsourdos, "Trajectory optimization for target localization with bearing-only measurement," *IEEE Trans. Robot.*, vol. 35, no. 3, pp. 653–668, Jun. 2019.
- [21] H.-S. Shin, J.-I. Lee, H. Cho, and A. Tsourdos, "Trajectory modulation guidance law for anti-ship missiles," in *Proc. AIAA Guid., Navigation, Control Conf.*, 2011, Paper AIAA 2011-6710.
- [22] T.-H. Kim, C.-H. Lee, and M.-J. Tahk, "Time-to-go polynomial guidance with trajectory modulation for observability enhancement," *IEEE Trans. Aerosp. Electron. Syst.*, vol. 49, no. 1, pp. 55–73, Jan. 2013.
- [23] D. V. Stallard, "Angle-only tracking filter in modified spherical coordinates," *AIAA J. Guid., Control, Dyn.*, vol. 14, no. 3, pp. 694–696, 1991.
- [24] S. Balakrishnan, "Extension to modified polar coordinates and applications with passive measurements," *AIAA J. Guid., Control, Dyn.*, vol. 12, no. 6, pp. 906–912, 1989.
- [25] A. G. Lingren and K. F. Gong, "Position and velocity estimation via bearing observations," *IEEE Trans. Aerosp. Electron. Syst.*, vol. AES-14, no. 4, pp. 564–577, Jul. 1978.
- [26] V. J. Aidala and S. C. Nardone, "Biased estimation properties of the pseudolinear tracking filter," *IEEE Trans. Aerosp. Electron. Syst.*, vol. AES-18, no. 4, pp. 432–441, Jul. 1982.
- [27] T. Song and J. Speyer, "A stochastic analysis of a modified gain extended Kalman filter with applications to estimation with bearings only measurements," *IEEE Trans. Autom. Control*, vol. AES-30, no. 10, pp. 940–949, Oct. 1985.
- [28] P. Del Moral, "Nonlinear filtering: Interacting particle resolution," *Markov Processes Related Fields*, vol. 2, no. 4, pp. 555–580, 1996.
- [29] S. He, J. Wang, and D. Lin, "Three-dimensional bias-compensation pseudomeasurement Kalman filter for bearing-only measurement," *AIAA J. Guid., Control, Dyn.*, vol. 41, no. 12, pp. 2678–2686, 2018.
- [30] S. E. Hammel and V. J. Aidala, "Observability requirements for three-dimensional tracking via angle measurements," *IEEE Trans. Aerosp. Electron. Syst.*, vol. AES-21, no. 2, pp. 200–207, Mar. 1985.
- [31] E. Fogel and M. Gavish, "Nth-order dynamics target observability from angle measurements," *IEEE Trans. Aerosp. Electron. Syst.*, vol. 24, no. 3, pp. 305–308, May 1988.
- [32] D. C. Woffinden and D. K. Geller, "Observability criteria for angles-only navigation," *IEEE Trans. Aerosp. Electron. Syst.*, vol. 45, no. 3, pp. 1194–1208, Jul. 2009.
- [33] S. Zhao, B. M. Chen, and T. H. Lee, "Optimal sensor placement for target localisation and tracking in 2D and 3D," *Int. J. Control*, vol. 86, no. 10, pp. 1687–1704, 2013.
- [34] N. A. Shneydor, *Missile Guidance and Pursuit: Kinematics, Dynamics and Control*. Amsterdam, The Netherlands: Elsevier, 1998.
- [35] T. L. Song and T. Y. Um, "Practical guidance for homing missiles with bearings-only measurements," *IEEE Trans. Aerosp. Electron. Syst.*, vol. 32, no. 1, pp. 434–443, Jan. 1996.
- [36] C.-H. Lee, T.-H. Kim, and M.-J. Tahk, "Biased PNG for target observability enhancement against nonmaneuvering targets," *IEEE Trans. Aerosp. Electron. Syst.*, vol. 51, no. 1, pp. 2–17, Jan. 2015.
- [37] H.-I. Lee, H.-S. Shin, and A. Tsourdos, "Weaving guidance for missile observability enhancement," *IFAC-PapersOnLine*, vol. 50, no. 1, pp. 15197–15202, 2017.
- [38] M. Tahk and J. Speyer, "Use of intermittent maneuvers for miss distance reduction in exoatmospheric engagements," in *Proc. Guid., Navigation Control Conf.*, 1989, Art. no. 3547.
- [39] H.-I. Lee, M.-J. Tahk, and B.-C. Sun, "Practical dual-control guidance using adaptive intermittent maneuver strategy," *AIAA J. Guid., Control, Dyn.*, vol. 24, no. 5, pp. 1009–1015, 2001.
- [40] M.-G. Seo and M.-J. Tahk, "Observability analysis and enhancement of radome aberration estimation with line-of-sight angle-only measurement," *IEEE Trans. Aerosp. Electron. Syst.*, vol. 51, no. 4, pp. 3321–3331, Oct. 2015.
- [41] D. Lee, M.-J. Tahk, and C.-H. Lee, "Optimal threshold of intermittent maneuver for target observability improvement," *Int. J. Aeronautical Space Sci.*, vol. 22, no. 4, pp. 911–922, 2021.
- [42] Y. Oshman and P. Davidson, "Optimization of observer trajectories for bearings-only target localization," *IEEE Trans. Aerosp. Electron. Syst.*, vol. 35, no. 3, pp. 892–902, Jul. 1999.
- [43] S. He, C.-H. Lee, H.-S. Shin, and A. Tsourdos, "Linear observability-enhancement optimal guidance law," in *Optimal Guidance and Its Applications in Missiles and UAVs*. London, U.K.: Springer, 2020, pp. 63–89.

- [44] D. Hull, J. Speyer, and D. Burris, "Linear-quadratic guidance law for dual control of homing missiles," *AIAA J. Guid., Control, Dyn.*, vol. 13, no. 1, pp. 137–144, 1990.
- [45] R. He, S. Chen, H. Wu, Z. Liu, and J. Chen, "Optimal maneuver strategy of observer for bearing-only tracking in threat environment," *Int. J. Aerosp. Eng.*, vol. 2018, pp. 1–8, 2018.
- [46] S. Zhao and D. Zelazo, "Bearing rigidity theory and its applications for control and estimation of network systems: Life beyond distance rigidity," *IEEE Control Syst. Mag.*, vol. 39, no. 2, pp. 66–83, 2019.
- [47] B. D. Anderson and J. B. Moore, *Optimal Filtering*, Chelmsford, MA, USA: Courier Corp., 2012.
- [48] T. Yoshikawa, "On discrete-time Kalman filter in singular case and a kind of pseudo-inverse of a matrix," *Int. J. Control*, vol. 15, no. 6, pp. 1157–1163, 1972.
- [49] G. Y. Kulikov and M. V. Kulikova, "Moore-Penrose-pseudo-inverse-based Kalman-like filtering methods for estimation of stiff continuous-discrete stochastic systems with ill-conditioned measurements," *IET Control Theory Appl.*, vol. 12, no. 16, pp. 2205–2212, 2018.
- [50] T. Balch and R. C. Arkin, "Behavior-based formation control for multi-robot teams," *IEEE Trans. Robot. Autom.*, vol. 14, no. 6, pp. 926–939, Dec. 1998.
- [51] R. Olfati-Saber, "Flocking for multi-agent dynamic systems: Algorithms and theory," *IEEE Trans. Autom. Control*, vol. 51, no. 3, pp. 401–420, Mar. 2006.
- [52] H. K. Khalil, *Nonlinear Systems*, 3rd ed. Englewood Cliffs, NJ, USA: Prentice-Hall, 2002.
- [53] C. H. Brighton and G. K. Taylor, "Hawks steer attacks using a guidance system tuned for close pursuit of erratically manoeuvring targets," *Nature Commun.*, vol. 10, no. 1, 2019, Art. no. 2462.
- [54] C. Aguilar-Ibanez, J. C. Martinez-Garcia, and A. Soria-López, "Bounded control based on saturation functions of nonlinear under-actuated mechanical systems: The cart-pendulum system case," in *Proc. 50th IEEE Conf. Decis. Control Eur. Control Conf.*, 2011, pp. 1759–1764.
- [55] T. Lee, M. Leok, and N. H. McClamroch, "Geometric tracking control of a quadrotor UAV on SE (3)," in *Proc. 49th IEEE Conf. Decis. Control*, 2010, pp. 5420–5425.
- [56] D. Mellinger and V. Kumar, "Minimum snap trajectory generation and control for quadrotors," in *Proc. IEEE Int. Conf. Robot. Autom.*, 2011, pp. 2520–2525.
- [57] M. Bangura, F. Kuipers, G. Allibert, and R. Mahony, "Non-linear velocity aided attitude estimation and velocity control for quadrotors," in *Proc. 16th Australas. Conf. Robot. Autom.*, 2015, pp. 1538–1543.
- [58] S. He, C.-H. Lee, H.-S. Shin, and A. Tsourdos, *Optimal Guidance and Its Applications in Missiles and UAVs*. Berlin, Germany: Springer Nature, 2020.
- [59] A. N. Bishop, B. Fidan, B. D. Anderson, K. Doğançay, and P. N. Pathirana, "Optimality analysis of sensor-target localization geometries," *Automatica*, vol. 46, no. 3, pp. 479–492, 2010.



Jianan Li received the B.Sc. degree in electromechanical engineering from the University of Macau, Macao, China, in 2015, and the M.Sc. degree in aerospace engineering from the Nanyang Technological University, Singapore, in 2018. He is currently working toward the Ph.D. degree with the Intelligent Unmanned Systems Laboratory, Westlake University, Hangzhou, China.

From 2018 to 2019, he was a Research Associate with the Air Traffic Management Research Institute, Singapore. His research interests include vision-based control and learning-based control with application to robotic systems.



Zian Ning received the B.Sc. degree in electrical engineering from Northwestern Polytechnical University, Xi'an, China, in 2015, and the M.Sc. degree in aeronautical engineering from Shanghai Jiao Tong University, Shanghai, China, in 2018. He is currently working toward the Ph.D. degree with the Intelligent Unmanned Systems Laboratory, Westlake University, Hangzhou, China.

His research interests include vision-based multi-robot cooperation, state estimation, and filtering.



Shaoming He received the B.Sc. and M.Sc. degrees from the Beijing Institute of Technology, Beijing, China, in 2013 and 2016, respectively, and the Ph.D. degree from Cranfield University, Cranfield, U.K., in 2019, all in aerospace engineering.

He is currently a Professor with the School of Aerospace Engineering, Beijing Institute of Technology, and also a recognized Teaching Staff with the School of Aerospace, Transport and Manufacturing, Cranfield University. His research interests include aerospace guidance, multitarget tracking, and trajectory optimization.

tory optimization.

Dr. He received the Lord Kings Norton Medal Award from Cranfield University as the Most Outstanding Doctoral Student in 2020.



Chang-Hun Lee received the B.S., M.S., and Ph.D. degrees in aerospace engineering from the Korea Advanced Institute of Science and Technology (KAIST), Daejeon, South Korea, in 2008, 2010, and 2013, respectively.

From 2013 to 2015, he was a Senior Researcher with Guidance and Control (G&C) Team, Agency for Defense Development (ADD), Daejeon. From 2016 to 2018, he was a Research Fellow with School of Aerospace, Transportation, and Manufacturing, Cranfield University, Bedford, U.K. Since 2019, he

has been with the Department of Aerospace Engineering, KAIST, where he is currently an Associate Professor. His recent research interests include advanced missile guidance and control, cooperative control for unmanned aerial vehicles, target tracking filter, deep learning, and aviation data analytics.

Dr. Lee is a Technical Editor of the *International Journal of Aeronautical and Space Science*.



Shiyu Zhao (Member, IEEE) received the B.Eng. and M.Eng. degrees from the Beijing University of Aeronautics and Astronautics, Beijing, China, in 2006 and 2009, respectively, and the Ph.D. degree from the National University of Singapore, Singapore, in 2014, all in electrical engineering.

From 2014 to 2016, he was a Postdoctoral Researcher with the Technion-Israel Institute of Technology, Haifa, Israel, and the University of California at Riverside, Riverside, CA, USA. From 2016 to 2018, he was a Lecturer with the Department of Automatic Control and Systems Engineering, University of Sheffield, Sheffield, U.K. He is currently an Associate Professor with the School of Engineering, Westlake University, Hangzhou, China. His research focuses on theories and applications of robotic systems.

From 2014 to 2016, he was a Postdoctoral Researcher with the Technion-Israel Institute of Technology, Haifa, Israel, and the University of California at Riverside, Riverside, CA, USA. From 2016 to 2018, he was a Lecturer with the Department of Automatic Control and Systems Engineering, University of Sheffield, Sheffield, U.K. He is currently an Associate Professor with the School of Engineering, Westlake University, Hangzhou, China. His research focuses on theories and applications of robotic systems.